photonics

MDPI

Review

Damping–Positioning Mechanisms in Segmented Mirror Systems: Principle, Integrated Design and Control Methods

Wuyang Wang [1,2], Qichang An [1,3,*] and Xiaoxia Wu [1,3,*]

[1] Changchun Institute of Optics, Fine Mechanics and Physics, Chinese Academy of Sciences, Changchun 130033, China; wangwuyang25@mails.ucas.edu.cn
[2] University of Chinese Academy of Sciences, Beijing 100049, China
[3] Jilin Provincial Key Laboratory of Intelligent Wavefront Sensing and Control, Changchun 130033, China
* Correspondence: anjj@mail.ustc.edu.cn (Q.A.); wuxiaoxia@ciomp.ac.cn (X.W.)

Abstract

Segmented telescopes face significant challenges in achieving high segment positioning accuracy under complex disturbances, which directly impact observational sensitivity and resolution. Conventional rigid actuators with limited bandwidth (e.g., Keck ~20 Hz) struggle to maintain control stability. Novel dual-stage actuators combining coarse and fine adjustment (e.g., voice coil motors) now achieve <8 nm precision over millimeter-level strokes. Moreover, their higher closed-loop bandwidth (e.g., TMT ~60 Hz) can ensure rapid settling without overshoot and robust suppression of high-frequency disturbances (e.g., pulsating wind and mechanical vibration). In parallel, system-level control strategies have been updated accordingly. Ground-based systems focus on real-time multimodal decoupling, while space-based systems emphasize non-contact vibration isolation and nested multi-loop control to achieve sub-arcsecond pointing stability. This review surveys the design and control strategies of damping–positioning mechanisms for segmented telescopes and discusses the key trade-offs among critical performance metrics, including resolution, stroke, and load capacity. Particular attention is given to the disturbance-sensitivity analysis and active damping techniques (up to ~50% vibration reduction) implemented in the ELT "hard" actuator approach. Future directions include cross-scale collaborative control, smart material applications, and AI-based adaptive parameter optimization, which together provide a technical pathway toward high-precision imaging in next-generation highly segmented telescopes.

Keywords: segmented telescopes; active optics; damping–positioning mechanism; dual-stage actuator; active damping; voice coil motor

Check for updates

Received: 25 September 2025
Revised: 27 February 2026
Accepted: 14 March 2026
Published: 17 March 2026

Copyright: © 2026 by the authors. Licensee MDPI, Basel, Switzerland. This article is an open access article distributed under the terms and conditions of the Creative Commons Attribution (CC BY) license.

1. Introduction

Astronomy is an observational science that fundamentally relies on large-aperture telescopes to collect faint light from the galaxy. For apertures smaller than 8.4 m, current technologies primarily include monolithic active thin primary mirrors and lightweight honeycomb-core composite mirrors. By contrast, for apertures larger than 8.4 m, the segmented mirror approach has become the dominant solution. By combining multiple smaller, more manufacturable and transportable segments into an effectively continuous, co-phased mirror, enhanced observational sensitivity and resolution can be achieved [1–6].

However, as aperture sizes increase, challenges, such as wind loads and vibration transmission from internal structures, which are beyond gravitational deformation and thermal effects, exacerbate the adverse impacts on imaging performance [7–10]. Steady-state wind components cause directional pointing deviations, whereas pulsating components excite structural vibrations that distort the shape of the primary mirror [11–14].

Thus, active optics (AO) have been developed to maintain imaging stability, becoming increasingly critical for segmented primary mirror co-phasing. In such systems, three actuators are typically installed on the backside of each segment to compensate for the out-of-plane piston–tip–tilt (PTT) errors [15]. At the same time, edge sensors (ES) measure the relative height differences between adjacent segments to implement feedback control [16]. Meanwhile, ES are periodically recalibrated using wavefront sensor (WFS) data to ensure long-term observational stability. Moreover, in-plane motions, such as translations (decenter) and clocking (rotation), induce discontinuous relative height variations that disrupt active control. Beyond the constraints of the passive support system (Whiffle-tree and radial support diaphragm) constraints, a full interaction matrix (IM) can be constructed to correlate segment displacements with ES signals, thereby reducing mirror adjustment errors [17].

Actuators play an important role in segment positioning and control. Conventional rigid actuators, with restricted bandwidth, exhibit insufficient dynamic response to high-frequency disturbances [18], prompting global research into coarse–fine collaborative voice-coil flexible actuators (VCAs). By capitalizing on the high bandwidth and excellent controllability of voice coil motors (VCMs), these novel actuators have successfully resolved this issue [19]. Nevertheless, in the design of dual-stage actuators, it is difficult to balance key performance metrics such as resolution, stroke, and load capacity. Trade-offs are still required. In terms of control, fast positioning with short settling time should be achieved without overshoot or residual vibrations. Although proportional-integral-derivative (PID) algorithms are still widely adopted for their simplicity and tunability, the control of larger-scale actuator arrays urgently requires the exploration of more suitable intelligent algorithms or hybrid control strategies to enhance overall robustness. Furthermore, increasingly complex disturbance quantities and frequency distributions [20] require the integration of targeted vibration measurements and isolation structures for precise modal identification and suppression, which are absent in most current positioning systems.

Considering the above-mentioned challenges, this paper reviews the design (Section 2) and control strategies (Section 3) of damping–positioning mechanisms for segmented telescopes. It highlights the trade-offs involved in actuator design, including precision, stroke, and load capacity, and examines the role of damping, particularly active damping, in mitigating overshoot and suppressing high-frequency resonance. The review also emphasizes the importance of advanced vibration analysis for selecting appropriate damping methods and control strategies, with the extremely large telescope (ELT) serving as a prime example of successful integration (Section 4). Finally, we aim to provide a reference for enhancing active AO capabilities to ensure imaging stability in next-generation segmented mirror systems.

2. Damping–Positioning Mechanism Design

2.1. Single-Stage Actuator

The Keck Telescope is the first segmented telescope, and Figure 1 illustrates the arrangement of its primary mirror and the associated AO system (WFS excluded).

The actuator of the Keck is shown in Figure 1d, where a servo motor drives a lead screw-nut assembly coupled with a 24:1 hydraulic reduction mechanism for axial displacement output. And a rotary encoder mounted on the servo motor enables precise step

control, achieving a resolution of 4.15 nm and a stroke of 1.1 mm [21–23]. This design provided a reference for subsequent segmented telescopes, such as the Gran Telescopio Canarias (GTC), Hobby–Eberly Telescope (HET), Southern African Large Telescope (SALT), and China's Large Sky Area Multi-Object Fiber Spectroscopic Telescope (LAMOST) (with two segmented mirrors: the aspheric corrector MA and the fixed spherical primary mirror MB). However, the unit cost of this system reaches approximately $7000 [24,25]. Similarly to hydraulic displacement scaling systems, flexure lever mechanisms with scaling ratios of 11.9:1, 12:1, and 10:1 have been adopted in HET, SALT, and LAMOST, respectively, to amplify the load capacity of actuators and improve positioning resolution. Even the Seimei Telescope in Japan, built in the 2020s, still employs such lever actuators (The detailed performance characteristics of these actuators are presented in Section 2.3 [26–31]. Although hysteresis and deadband issues were subsequently resolved via backlash elimination mechanisms [32,33], this single-stage drive still struggles to address "the error chasing" problem—specifically, its response speed lags behind the error update frequency. This drawback stems from the fundamental constraints imposed by its low bandwidth and inherent rigidity.

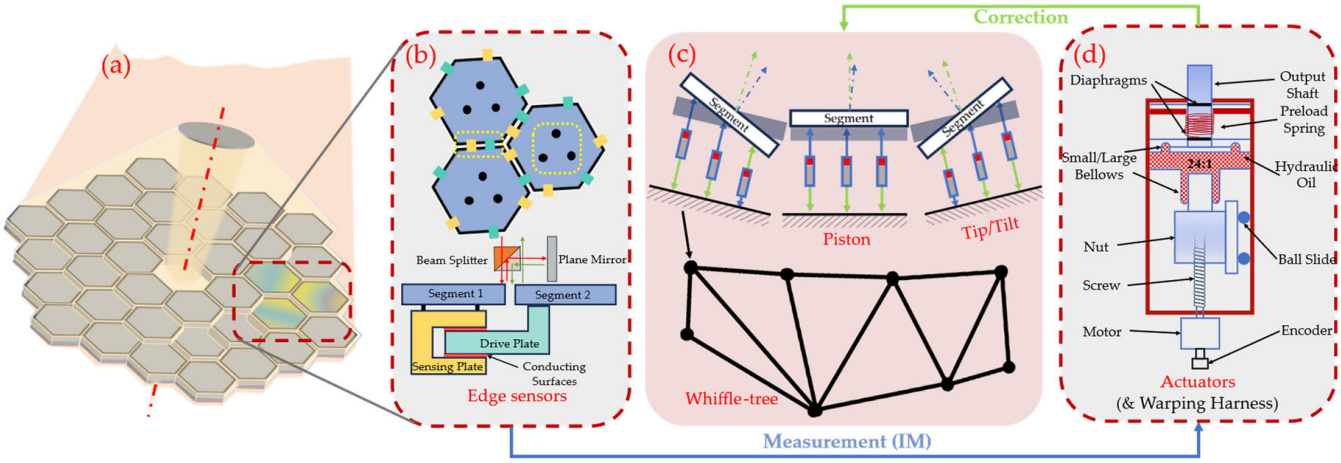

Figure 1. (**a**) The arrangement of Keck primary mirror; (**b**) Keck ES, where one drive plate is used for signal excitation, and the other for sensing the relative displacement between segments; (**c**) Schematic diagram of segmented mirror adjustment and the Whiffle-tree passive sup-port structure; (**d**) Keck actuators compensate for rigid-body PTT errors, while the warping harness actively corrects low-order surface figure errors (e.g., astigmatism, not shown) [23].

At present, hydraulic actuator technology is undergoing significant innovation. In 2025, Zhan et al. [34] proposed a Piezo-Hydraulic actuator for fast steering mirror (see Figure 2). By employing a hydraulic micro-displacement amplifier (HMDA) based on Pascal's law, the actuator achieves high-precision motion amplification. Compared with the Keck actuator, this design attains a displacement amplification ratio of up to 12.61:1 while maintaining a compact form factor. With dimensions of Φ44 mm × 71 mm, it can support a 2 kg mirror segment and exhibits a first-order resonance frequency as high as 1356 Hz. Leakage issues are effectively mitigated through the use of a flexure piston and a silicon membrane. Driven at 150 V, the actuator delivers an output stroke of 104.9 μm, offering a practical solution to the long-standing trade-off between large stroke and high bandwidth in precision actuation systems (e.g., segmented mirror positioning system).

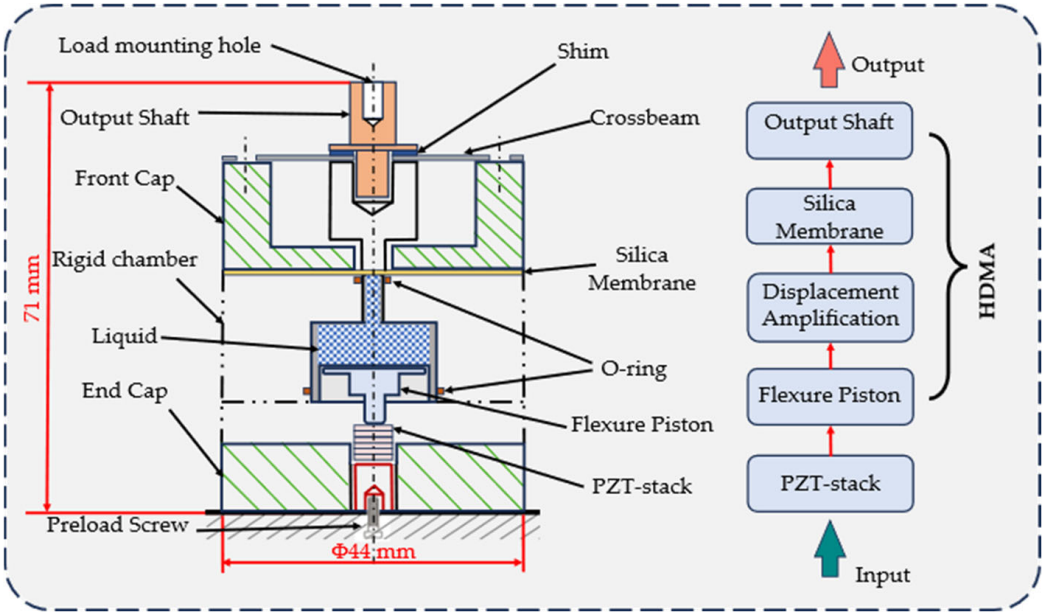

Figure 2. Structure of the Piezo-Hydraulic actuator and displacement output path [34].

2.2. Dual-Stage Actuator

For next-generation segmented telescopes, such as the Thirty Meter Telescope (TMT) and the ELT, we summarize the disturbances affecting the co-phasing maintenance of their segmented primary mirrors [24]:

- Dominant low-frequency, large-scale deformations caused by gravity, thermal effects, and steady wind, primarily controlled by AO control loops;
- High-frequency small-displacement vibrations induced by internal mechanical vibrations and external pulsating wind, requiring high-bandwidth local control at the actuator level.

In response to these disturbances, a two-stage actuator architecture was developed and continuously refined. The coarse stage provides millimeter-scale stroke for rapid initial positioning, while the fine stage, with high bandwidth, enables nanometer-level precision and fast dynamic response. According to the number of drive motors, current actuators are mainly classified as "decoupled" actuators and "dual-drive" actuators.

2.2.1. Decoupled Actuator

This class of actuators enables both coarse and fine segment positioning using a single stepper motor. A representative example is the James Webb Space Telescope (JWST) actuator. Each segment of the JWST is equipped with six customized displacement actuators developed by Ball Aerospace & Technologies Corp, Boulder, CO, USA, as shown in Figure 3. The actuator integrates a coarse-motion transmission coupling shaft (Figure 3a) with a fine-position compound flexure mechanism (Figure 3b,c). The coarse stage employs a gear-coupled lead screw with a preloaded spring to eliminate backlash and increase load capacity, while the fine stage uses an eccentric cam-driven flexure to enhance displacement resolution, with a torsional stabilizer ensuring purely axial motion. This architecture achieves a 21 mm stroke and 7 nm resolution. To accommodate the cryogenic space environment, all friction-prone components are treated with dry-film lubrication to prevent lubricant freezing at extremely low temperatures [35–38].

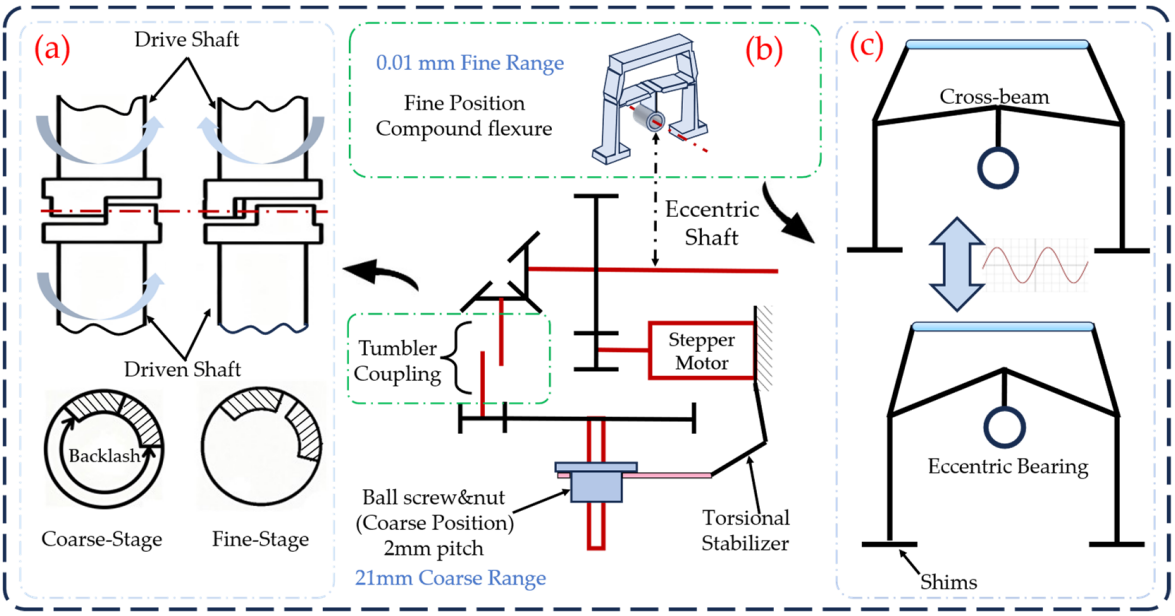

Figure 3. Specific structure of JWST actuator. (**a**) Coarse-motion transmission coupling shaft (The specific functions and the process of coarse–fine conversion are detailed in the Section 3); (**b**) Simplified compound flexure; (**c**) Principle of fine-stage flexure: The flexure has an approximately A-shaped geometry. Motion of the cross-beam induces elastic deflection of the side beams, resulting in a reduced vertical displacement of the flexure gauge. The cross-beam is driven by an eccentric camshaft actuated by a geared motor, producing a quasi-sinusoidal output displacement. Owing to the composite geometry of the flexure, the sinusoidal motion is geometrically modulated. The fine-motion range can be tuned by adjusting the shim thickness beneath the flexure feet, where a 0.1-mm shim change corresponds to approximately 1 μm of fine displacement (100:1) [38].

Building on the JWST actuator concept, Wu [39] also proposed a decoupled coarse–fine actuator driven by a single TUNYO 35-mm decelerated stepper motor with a brake, achieving 3 nm positioning precision over a 20 mm stroke. Dynamic simulations demonstrate a seamless transition during the coarse–fine switching process. Upon approaching a commanded position, the actuator exhibits a negligible overshoot ratio on the order of parts per million relative to the target displacement before converging precisely to its final state. This minute deviation, which includes a deliberate component for backlash management as discussed in Section 3.1.1, occurs without observable oscillation or residual vibration. This behavior reflects the combined effects of three primary damping mechanisms incorporated in the decoupled actuator:

- effective structural damping of the flexure hinges at the output stage, which contributes to micro-vibration attenuation through elastic energy dissipation;
- Frictional damping introduced by anti-backlash flexure sheets and mechanisms in the coarse–fine transmission chain;
- Braking damping provided by the stepper-motor brake during positioning and locking.

It should be noted that all damping mechanisms discussed above are inherently passive, relying on structural, frictional, and braking-induced energy dissipation rather than active feedback control. By contrast, active damping strategies are more commonly implemented in dual-drive actuator architectures, where additional actuation authority and control bandwidth enable closed-loop vibration suppression.

2.2.2. Dual-Drive Actuator

Dual-drive actuators employ two independent drive units to separately realize coarse and fine positioning, with the fine stage most commonly implemented using a VCM. This

actuator architecture has been adopted in 30 m TMT and 39 m ELT [24,40]. In the TMT segment actuator, a VCM is employed as the fine-stage drive to enable nanometer-level positioning (Figure 4a). To compensate for the limited force capability of the VCM, a self-adjusting spring–lever load-sharing mechanism is introduced. The lever fulcrum adopts C-flex bearings, which eliminate friction and backlash while providing passive structural damping against lateral and micro-vibrational disturbances. In addition to passive damping, active damping is realized through closed-loop control of the VCM. Real-time displacement feedback allows dynamic modulation of the VCM current, enabling control forces to act synergistically with structural damping and thereby achieve integrated vibration suppression and precise segment pointing. As a result, the actuator provides an effective stroke of up to 4.3 mm, satisfying the TMT requirement (>1.2 mm) derived from the maximum expected gravity-induced segment deformation. It achieves a resolution of 1.2 nm and a tracking error below 5 nm RMS at tracking speeds of ±2000 nm/s, while reducing the vibration response in the resonance frequency band by approximately one order of magnitude compared with the rigid actuators used in Keck [40,41].

In the ELT Position Actuator (PACT), a brushless DC motor is adopted for smoother coarse-stage motion to avoid stepper motor jump discontinuities. The fine adjustment considers two options:

- "Soft" approach: VCM-driven flexure design with flat spring load unloading (Figure 4b) enables low-friction, fast actuation and minimizes hysteresis [19];
- "Hard" approach: A piezoelectric ceramic-driven rigid piezoelectric actuator (PZT actuator) provides high stiffness and strong rejection of steady wind disturbances [42].

Testing on the M1 platform by ESO shows that the PACT actuator provides a stroke of 15 mm with a positioning error of 1.4 nm RMS. A feedback controller, specially designed by TNO for this actuator, enables a VCM-based design with a closed-loop bandwidth of 100 Hz and an axial stiffness resonance frequency above 120 Hz. Experimental results demonstrate that the actuator effectively suppresses ground vibrations and wind disturbances, with a suppression factor exceeding 10^3 [42–44]. To provide a more comprehensive overview of the actuator designs adopted by these extremely large telescopes, Table 1 summarizes the specific design parameters of the two-stage actuators for TMT and ELT. Notably, the final ELT PACT, whose serial production has been awarded to Physik Instrumente (PI) GmbH & Co., KG, Karlsruhe, Germany by ESO [45], adopts a "hard" concept ensuring high passive stiffness and relying on positive position feedback (PPF) for active damping (see Section 4 for details).

Table 1. Comparison of actuator design parameters for TMT and ELT [41–45].

Design Parameter	TMT	ELT
Actuator Architecture	Soft actuator: Voice-coil (fine) + Stepper motor with spring offloading (coarse)	Hard actuator: Piezo actuator (fine) + Brushless DC-motor with harmonic drive & roller screw (coarse)
Total Stroke	>4.3 mm	±5 mm (10 mm total)
Tracking Error (RMS)	<5 nm	2 nm
Resolution	1.2 nm	sub nanometer
Tracking Speed Range	±2000 nm/s	0–450 nm/s
Max Slew Rate	≥50 µm/s	100 µm/s
Open-loop Axial Stiffness	0.16 N/µm	>20 N/µm

Table 1. *Cont.*

Design Parameter	TMT	ELT
Closed-loop Bandwidth	60 Hz	~30 Hz (Piezo fine stage); 5–6 Hz (Motor coarse stage)
Transverse Stiffness	>4 N/μm	-
Max Load Capacity	750 N (Axial operating)	2.2 kN (Max Compression); 3.5 kN (Max Tension)
Weight	<7 kg	-
Power Dissipation	<2 W tracking (<1 W goal)	-
Lifetime/Reliability	>50 Years/MTBF > 300,000 h	30 Years/350,000 h
Damping Strategy	Closed-loop PID control of voice-coil	PPF on Piezo actuator

Dual-stage actuators, with their specific characteristics, are widely adopted in large-aperture telescopes like TMT and ELT, but they are also increasingly being used in smaller systems due to their versatility and precision. For example, the 1.5 m Prototype Segmented Mirror Telescope (PSMT) incorporates a VCM-driven flexible actuator with a disc flexure spring (Figure 4c) [46,47]. This design effectively prevents radial deviation and isolates the output shaft to achieve the required "flexible" performance. With a combined position, unloading, and tuning loop using relay PID tuning, it meets the 350 nm/s tracking rate requirement with an error of just 10.15 nm. To prevent negative mirror pressure during tip/tilt corrections, Liu [48] integrated low-stiffness negative-pressure springs with the VCM, enabling tensile-force adaptation. This innovation achieved an impressive 2.5 nm resolution (Figure 4d).

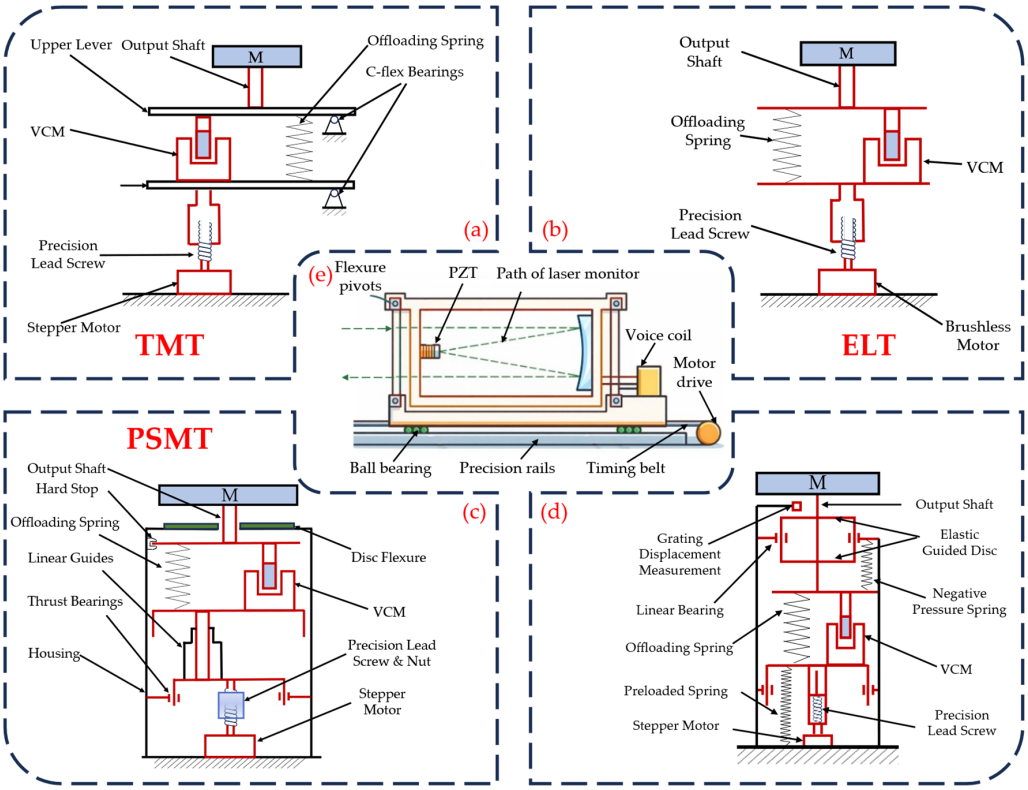

Figure 4. Various structural schematic diagrams of dual-drive actuators: (**a**) TMT actuator [41]; (**b**) VCM-based actuator for the ELT [19]; (**c**) PSMT actuator [46,47]; (**d**) Actuator designed by Liu [48]; (**e**) Three stage (PZT, Voice Coil, Motor) optical delay line [49,50].

2.2.3. Three-Stage Delay Line Actuation

In the classical moving delay line architecture derived from the Mark III interferometer [49,50], optical path control is realized through a nested three-stage actuation scheme that distributes precision, bandwidth, and stroke across different scales (see Figure 4e). Fine delay correction is achieved by a PZT-driven retroreflecting mirror, providing subwavelength resolution with a typical stroke of several tens of micrometers and bandwidths in the kilohertz range. To avoid saturation of this fine stage, a voice-coil-driven intermediate stage supplies millimeter- to centimeter-scale continuous motion with bandwidths on the order of tens to hundreds of hertz, recentering the PZT while preserving smooth, backlash-free dynamics. Serving as the critical bridge between fine and coarse control, the voice-coil stage absorbs mid-frequency disturbances and slow drifts, effectively decoupling high-speed optical correction from large-stroke positioning. Finally, a linear-motor-driven coarse stage delivers meter-scale delay adjustment at low bandwidth for geometric path compensation.

Essentially, its function is the same as that of actuators, outputting minute displacements, but the three-stage actuator has not yet seen practical application.

2.3. Trade-Offs in Key Performance Metrics

To more clearly analyze the development trends of damping–positioning mechanisms, the key performance metrics of the representative actuators discussed above, including resolution, stroke, load capacity (characterized by segment mass), and actuator bandwidth, are summarized in Table 2. In addition, the main advantages and limitations of the two actuator architectures are distilled and compared in Table 3. Here, it is necessary to distinguish between the local operational bandwidth of the actuators and the global AO closed-loop bandwidth. For conventional single-stage actuators, the global AO loop is typically constrained to sub-hertz levels (e.g., ~0.5 Hz for Keck) to avoid control–structure interaction (CSI) [51]. In contrast, dual-stage actuators in TMT and ELT decouple these functions: their fine-stage components provide high local bandwidth (60–100 Hz) specifically for active damping and high-frequency disturbance rejection, while the global system-level correction remains conservative to ensure overall structural stability.

Single-stage actuators employ a single drive source and are characterized by structural simplicity. Their output resolution is enhanced by a large mechanical reduction ratio. However, for a given scaling ratio, obtaining sufficient output stroke requires a correspondingly large input displacement from the lead screw, which inevitably increases cumulative transmission error. As a result, the achievable stroke is typically limited to less than 2 mm, making it challenging to simultaneously meet the demands for both large stroke and high precision. Fortunately, actuators based on HMDA–PZT stack architectures (Zhan et al. [34]), combined with flexure piston and silicone-membrane structures, provide a viable means of alleviating this trade-off for rigid actuators. In parallel, the ELT has explored the application of active damping on PZT-based actuators to compensate for their limited capability in suppressing high-frequency resonances. These approaches will be discussed in more detail in Section 4.1.

By contrast, dual-stage actuators decouple stroke and precision by assigning them to separate drive units. As demonstrated by the JWST actuator, strokes of up to 20 mm can be achieved, representing more than an order-of-magnitude increase over single-stage designs, while maintaining an average positioning precision better than 8 nm. This architecture therefore provides a more balanced solution to the competing performance requirements. In addition, the maturity and standardization of VCM technology enable the extensive use of industrial off-the-shelf components. Consequently, the unit cost of actuators for TMT and the ELT PACT is controlled below $2000 and €4000, respectively,

significantly lower than that of the early Keck actuators (~$7000), which is advantageous for large-scale deployment [23,24]. Nevertheless, the fundamental mechanical simplicity of single-stage architectures remains a distinct advantage. Their streamlined design avoids nested mechanisms and redundant sensors to offer a more compact physical footprint. As actuator technology has matured since the early development stages, the production costs of single-stage designs have also dropped significantly, rendering them a highly cost-effective solution for telescopes with less demanding dynamic requirements.

Table 2. Comparison of conventional single-stage actuators and dual-stage actuators.

Structure	Project		Resolution /nm	Stroke/mm	Load/kg	Inertia/ (kg·m^2)	Bandwidth/Hz	
							Local	Global (AO)
Single-stage Actuators	Keck (10 m level)		4.15	1.1	400 (hexagon)	135.00	~20	~0.2
	GTC (10 m level)		1.19	1.6	470 (hexagon)	176.74	50–100	2–5
	HET (10 m level)		18	1.83	~100 (hexagon)	~13.78	-	-
	SALT (10 m level)		30	1.66	~100 (hexagon)	~14.02	-	
	LAMOST (4 m)	MA	4.45	4	~50 (hexagon)	~6.30	-	
		MB	11	25	~150 (hexagon)	~18.91		
	Seimei (3.8 m)		0.86	1	~67 (petal)	inner ring ~4.84 outer ring ~6.78		
Dual-stage Actuators	JWST (6.5 m)		7	21	20 (hexagon)	4.69	-	
	TMT (30 m)		1.2	4.3	~180 (hexagon)	~38.88	small-signal >25 closed loop 60	~1
	ELT (39 m)	"Soft"	1.4	15	~250 (hexagon)	~51.04	100	0.5–1
		"Hard"	sub nanometer	10			~30	

Table 3. Advantages and disadvantages of two types of actuator designs.

Structure	Advantages	Disadvantages
Single-stage Actuators	Simpler and more compact structure; User-friendly operation;	Mutually exclusive stroke and precision; Friction, backlash, hysteresis; Limited bandwidth and poor dynamic response to high-frequency disturbances;
Dual-stage Actuators	High-bandwidth VCM-based fine positioning stage; Enhanced high-frequency disturbance suppression through combined passive and active damping;	Coordination challenges; Auxiliary unloading components required;

Overall, both single-stage actuators and two-stage actuators are advancing with the times and actuator architectures are evolving from traditional electro-hydro-mechanical solutions toward non-contact VCM-based and PZT-based designs, and even combined three-stage actuation integrating both technologies (delay line [49,50]).

Next, we further discuss that the adoption of flexible actuators introduces inherent system-level trade-offs beyond the primary performance metrics. While VCM-based designs offer high bandwidth and strong damping capability for suppressing high-frequency disturbances from pulsating wind and internal micro-vibrations, their reduced structural

stiffness weakens resistance to steady-state wind loads, which are a dominant disturbance source in large ground-based telescopes [10–19]. In contrast, rigid actuators are more effective in counteracting low-frequency and quasi-static disturbances. Additionally, the limited output force of VCMs constrains actuator load capacity, often requiring auxiliary unloading mechanisms to maintain precision, which affects system scalability. Larger segment sizes can reduce overall control complexity (fewer segments for the same aperture diameter), making higher actuator load capacity desirable at the system level. Furthermore, dual-drive architectures introduce dynamic coupling between coarse and fine stages, which also require advanced decoupling and coordination algorithms, increasing both computational cost and tuning complexity.

To sum up, beyond structural evolution, the collaboration between dual-stage actuators and improvements in system-level control architectures is both inevitable and crucial.

3. Actuator Collaboration and System-Level Control

3.1. Dual-Stage Actuator Collaboration and Local Control Architecture

In large-aperture segmented mirror systems, the coordination of actuators is crucial for achieving high-precision segment positioning. Decoupled actuators typically use independent coarse and fine adjustment mechanisms, effectively minimizing the impact of coarse adjustments on fine resolution. This design reduces mutual interference and enhances system stability and response speed, particularly in the face of high-frequency disturbances and system-level vibrations. However, dual-drive actuators, while offering similar advantages, introduce a unique challenge due to the dynamic interaction between the coarse and fine stages. The coarse stage, with its larger strokes, may induce residual motion that affects the fine stage, leading to potential oscillations and overshoot. This interaction is especially problematic during coarse-to-fine switching when fine adjustments need to be precise. Therefore, effective collaboration between the coarse and fine stages is critical, and sophisticated control algorithms are required to minimize oscillations and ensure smooth operation.

3.1.1. Actuator Correction Process

Decoupled actuators with "rise–overshoot/fall–undershoot" strategy [35–39]

See Figures 3 and 5a. During coarse adjustment, the motor drives the reducer and bevel gear set, transmitting torque to the coarse transmission coupling. With the active and passive shafts engaged, the downstream gear train and ball screw move synchronously to generate a large-stroke linear output for rapid positioning.

- Coarse-to-fine transition: To guarantee a smooth transition to the fine stage, the coarse motion follows a deliberate "rise–overshoot/fall–undershoot" strategy. When the fine-stage eccentric output is in the rising phase, the coarse stage slightly overshoots the target by one resolution unit; when in the falling phase, it undershoots by the same margin. This intentional bias ensures that subsequent reverse motion remains fully within the designed backlash range [39].
- For fine adjustment, the motor reverses its rotation. Owing to the specially designed coupling, a large intentional reverse backlash is introduced, causing the active and passive shafts to disengage. The ball screw and coarse stage are therefore mechanically isolated and remain stationary. In this decoupled state, only the eccentric bearing coaxial with the bevel gear drives the flexible lever, producing nanometer-level displacement through a high reduction ratio (~100:1).

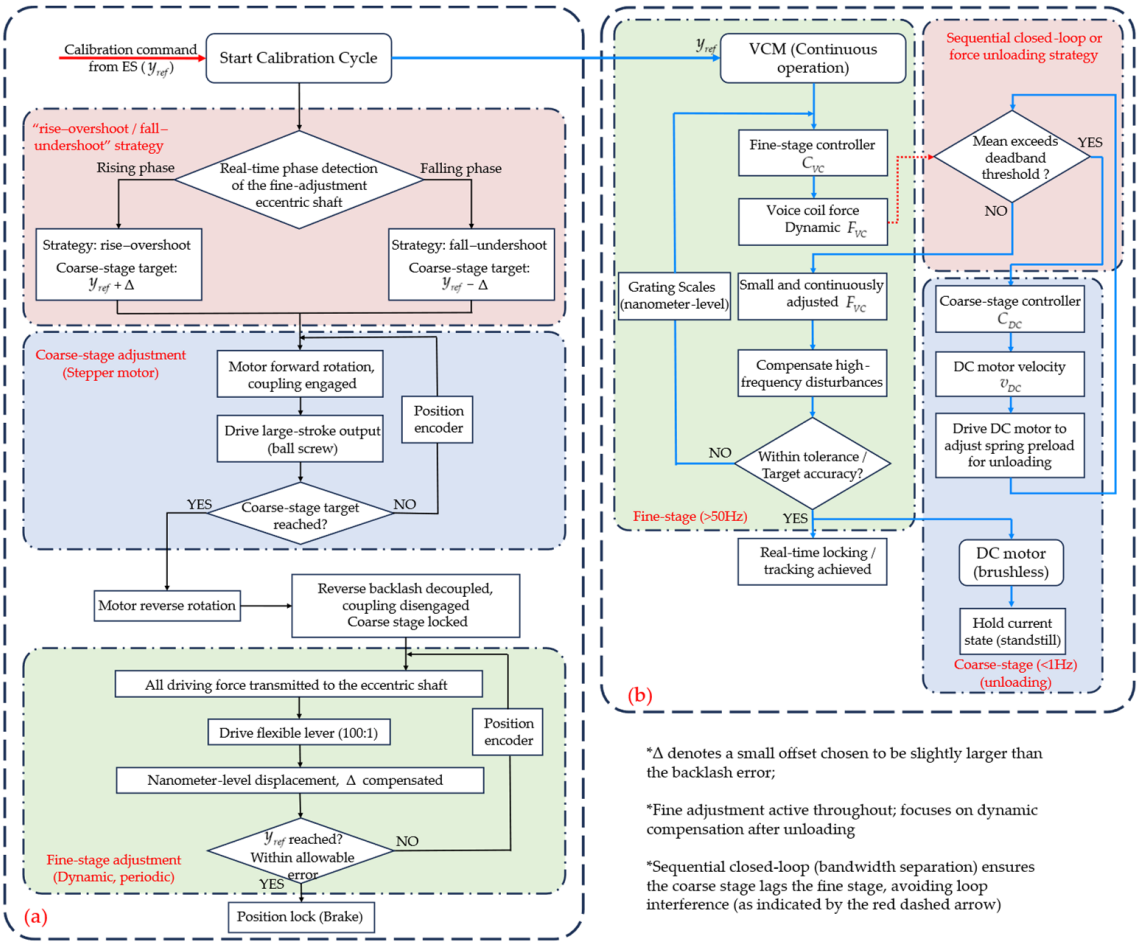

Figure 5. Operational flowchart of the dual-stage actuator. (**a**) Decoupled actuator; (**b**) Dual-drive actuator (based VCM). In general, when the velocity command is nonzero, F_{VC} deviates from the deadband threshold and the DC motor assists in unloading. During this process, VCM braking is achieved by applying a reverse velocity command, while the corresponding DC motor adjustment is computed by C_{DC}. (* denotes additional notes).

The pre-arranged over-/under-shoot in the coarse stage allows the fine motion to compensate directly for the residual error without re-engaging the coarse transmission, thereby avoiding limit cycling and suppressing oscillation during coarse–fine switching.

Dual-drive actuators with sequential closed-loop/force unloading strategy [41–44,52]

See Figures 5b and 6. Upon receiving the reference command y_{ref} from the telescope control system (ES or WFS of AO), both the coarse and fine (VCM) control loops operate in closed loop. And they are governed by a sequential closed-loop strategy with separated bandwidths. The coarse stage operates in the low-frequency range (below 1 Hz) for large-stroke positioning, while the fine stage functions at high bandwidth (above 50 Hz) to correct residual errors and suppress high-frequency disturbances. This bandwidth partitioning minimizes cross-coupling between stages and forms a closed-loop MIMO control architecture.

- Coarse stage (low-bandwidth load unloading): The coarse-stage controller C_{DC} uses the VCM force output F_{VC} as feedback and, through a low-pass filter with a cutoff frequency below 1 Hz, adjusts the DC motor velocity v_{DC} to drive the output shaft toward the reference position (position command) y_{ref}. The equivalent plant for the coarse stage, derived from the closed fine-loop, is:

$$H_{\mathrm{eq}}(s) = -\frac{C_{\mathrm{VC}}(s)}{1 + C_{\mathrm{VC}}(s)H_{\mathrm{VC}}(s)} \cdot H_{\mathrm{DC}}(s) \tag{1}$$

where H_{VC} and H_{DC} represent the transfer functions from F_{VC} to y and from v_{DC} to y, respectively. $H_{\mathrm{DC}}(s) \approx K_{DC}/s$ (integrator behavior for low frequencies, K_{DC} is the DC motor gain). When the average value of F_{VC} or VC current (the Lorentz-force principle) deviates from the zero position (exceeding a threshold), it indicates that the gravitational load is not completely balanced. When y approaches y_{ref}, C_{DC} reduces v_{DC} until the VC current drops below this threshold, at which point the DC motor halts.

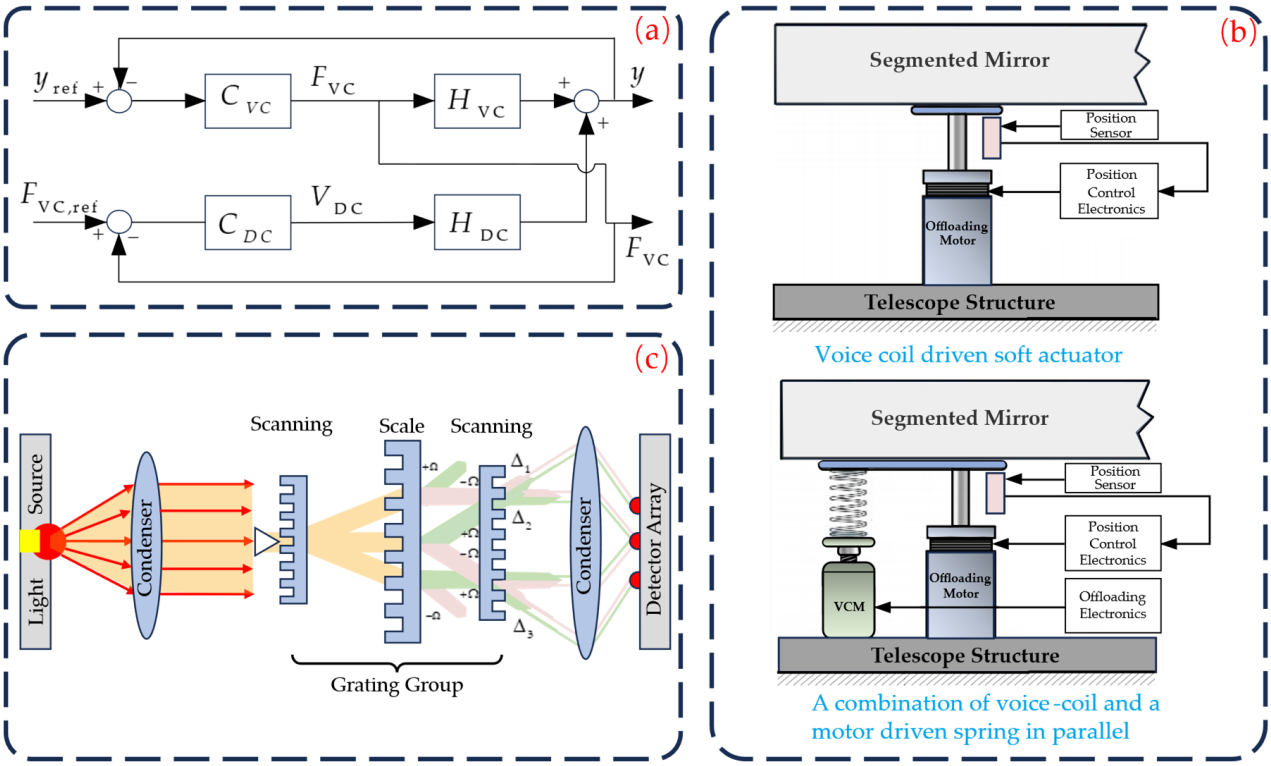

Figure 6. Dual-drive actuator simplified system and control model: (**a**) Block diagram of dual-drive coarse–fine dual-stage combined control; (**b**) The concept of a flexible actuator using a parallel combination of a voice coil and a offloading motor-driven spring is proposed to achieve minimal power consumption [43]; (**c**) Principle of grating encoder (position sensor) [47].

- Fine-stage (high-bandwidth position tracking): Once the coarse stage unloading is completed, the fine stage will be liberated to focus on dynamic compensation. The fine-stage controller C_{VC} can adopt a PID structure augmented with lead-lag compensation and notch filters to suppress structural resonances. The transfer function of $C_{VC}(s)$ is parameterized as:

$$C_{\mathrm{VC}}(s) = K_p \cdot \frac{1 + \tau_1 s}{1 + \tau_2 s} \cdot \frac{1 + \frac{2\zeta}{\omega_n}s + \left(\frac{s}{\omega_n}\right)^2}{1 + \frac{2\zeta_d}{\omega_d}s + \left(\frac{s}{\omega_d}\right)^2} \tag{2}$$

where K_p is proportional gain; τ_1 and τ_2 are lead-lag time constants; ω_n is resonance frequency of the notch filter. At the same time, the fine-stage loop uses the internal grating encoder (see Section 3.1.2) for feedback.

- Backlash compensation: Using force feedback, the coarse DC stage linearizes friction via a local velocity controller and decelerates near y_{ref} to avoid "stick-slip". The contactless fine-stage VCM then takes over for precise positioning, making any small

"downhill" motions [44] from coarse self-locking negligible. This is akin to a "rise–overshoot/fall–undershoot" strategy, implemented via force feedback.

In this design, the fine stage acts as the primary controller, continuously responding to all position commands and disturbances to ensure dynamic accuracy. The coarse stage is the secondary controller, operating at a much slower speed and event-driven—its actions are triggered only when the fine-stage load persists away from zero, rather than simply mirroring fine-stage motion. This sequential closed-loop operation, also referred to as the force-unloading strategy, allows the coarse stage to handle stroke and power optimization while the fine stage maintains nanometer-level tracking accuracy throughout the switching and adjustment process [43].

Closed-loop stability verification of the ELT system [43] shows that all open-loop frequency responses $H_i(j\omega)C_i(j\omega)$ (for $i = \mathrm{VC},\ \mathrm{DC}$) maintain a 6 dB gain margin, i.e., the Nyquist plots do not encircle $(-1, 0)$. Quantitative tests indicate that, at a velocity command of 1.2 μm/s and under 0.55 N RMS wind disturbance, the system achieves 1.4 nm RMS tracking error, with VCM power consumption below 7.6 mW RMS.

3.1.2. Actuator Local Feedback

During the dual-stage actuator calibration process, real-time feedback from high-precision displacement sensors, such as grating encoders and Linear Variable Displacement Transducers, is critical for ensuring steady-state accuracy. Compact, miniature grating-based displacement measurement systems with high resolution are therefore widely adopted in industrial motion control (Figures 5b and 6c). For example, the TMT actuator integrates a displacement sensor developed by MicroE Systems (Mercury II), Bedford, MA, USA on its output shaft. This laser-based grating encoder decodes positional variations into 32-bit digital signals through interference fringe detection and interpolation, achieving a resolution of 1.2 nm and enabling full closed-loop position control [41]. Similar high-precision feedback schemes have also been implemented in the Gemini M2TS secondary mirror system [53]. In addition, Liu et al. [48] employed Renishaw ATOM DX gratings with a 20 μm glass linear scale in a VCA design, attaining a maximum resolution of 2.5 nm. However, high-frequency noise and signal latency inherent to grating encoders may degrade dynamic performance. Accordingly, the following methods are adopted to improve steady-state behavior:

- Grating-scale calibration: Grating scales are inherently affected by manufacturing-induced mark-position errors. Calibration against higher-precision displacement references, such as laser interferometers, enables these errors to be characterized and compensated using lookup tables over the actuator travel range;
- Multisensor fusion with Kalman filtering: Combining grating scales, strain gauges, and accelerometers enables Kalman-filter-based multisensor fusion. Accelerometers capture high-frequency dynamics, strain gauges suppress low-frequency drift, and grating scales provide absolute position reference;
- Adaptive PID parameter tuning: Adaptive PID schemes adjust controller gains according to the real-time position error. High-gain tuning is applied in the large-error regime to accelerate convergence, while low-gain tuning is used near steady state to avoid overshoot and reduce settling time.

3.1.3. Interaction Matrix and Edge Sensor Drift Issues

Beyond how individual actuators are calibrated and controlled, it is equally important to determine what is being corrected, i.e., y_{ref} applied to each actuator. In segmented mirror systems, these references are generated by the AO system based on ES measurements and the IM constructed from them (see Figure 5).

The IM establishes the linear mapping between segment rigid-body motions and the relative height differences and dihedral angles measured by adjacent edge sensors. Following the approach adopted in systems such as LAMOST [54,55], the IM is constructed from a quasi-static mechanical model and refined through experimental identification, yielding a sensor–actuator relationship whose dimensionality scales with the number of segments, sensors, and actuators. In operation, discrepancies between measured and ideal ES outputs are projected through the pseudo-inverse of the IM to estimate segment displacements, which are then converted into y_{ref}.

To ensure robustness, the pseudo-inverse is typically obtained via singular value decomposition (SVD), allowing unobservable or weakly observable modes to be treated explicitly. In addition to the global piston mode, global clocking or torsional modes of the segmented mirror assembly are also suppressed, as they cannot be reliably sensed by ES measurements alone [56]. Mode-dependent gain constraints are further applied to mitigate sensitivity to modeling errors.

Long-term drift in the ES results from thermal variations, structural relaxation, and sensor aging. To mitigate this, periodic recalibration (every 3–4 weeks at Keck [57,58]) using WFS [59–62] or laser metrology systems [56,63–65] updates the global reference state. Design improvements such as the use of low-thermal-expansion materials (e.g., ceramics in the ELT ES [66]), differential measurement to suppress common-mode drift, protective sealing, and advanced signal processing reduce low-frequency sensor drift [54,67–70]. In this hierarchical scheme, IM-based AO control provides low-frequency, system-level reference commands, while actuator-level closed-loop control compensates for high-frequency residuals.

As the system scale increases (e.g., sensor-actuator 2772 × 1476 for TMT), the growing dimensionality of the IM and the resulting computational burden, together with CSI effects between actuators and sensors, pose fundamental challenges to stability and scalability. These issues motivate the advance of system-level control strategies, which are discussed in the following Section 3.2.

3.2. System-Level Control of Segmented Mirrors

3.2.1. Ground-Based Telescope

Keck [51,71–73]

The Keck provided the first large-scale demonstration of active optical control in astronomical observations. Each 10 m primary mirror consists of 36 segments, each independently controlled by 3 actuators, with 168 differential ES forming a closed-loop feedback network (see Figures 1 and 7a). Operating at a 40 ms sampling period, a pure integral common-mode control algorithm aligns inter-segment PTT errors to ~10 nm, producing an effectively continuous parabolic wavefront. This multi-degree-of-freedom coordination enables real-time compensation of low-frequency optical path errors from gravitational flexure and thermal drift, while broad-band resonances between 5 and 200 Hz, particularly CSI near 22 Hz, limit the control bandwidth to ~0.5 Hz, restricting high-frequency disturbance rejection and motivating modal decoupling strategies for subsequent large segmented telescopes. At the wavefront sensing level, Keck introduced the Phasing Camera System (PCS), which performs hierarchical correction of common-mode segment errors through multi-mode coordination. The Phasing Camera System has been successfully operated on Keck I and II for over 30 years, completing more than 1000 mirror phasing operations and demonstrating the long-term reliability of segmented mirror control and metrology.

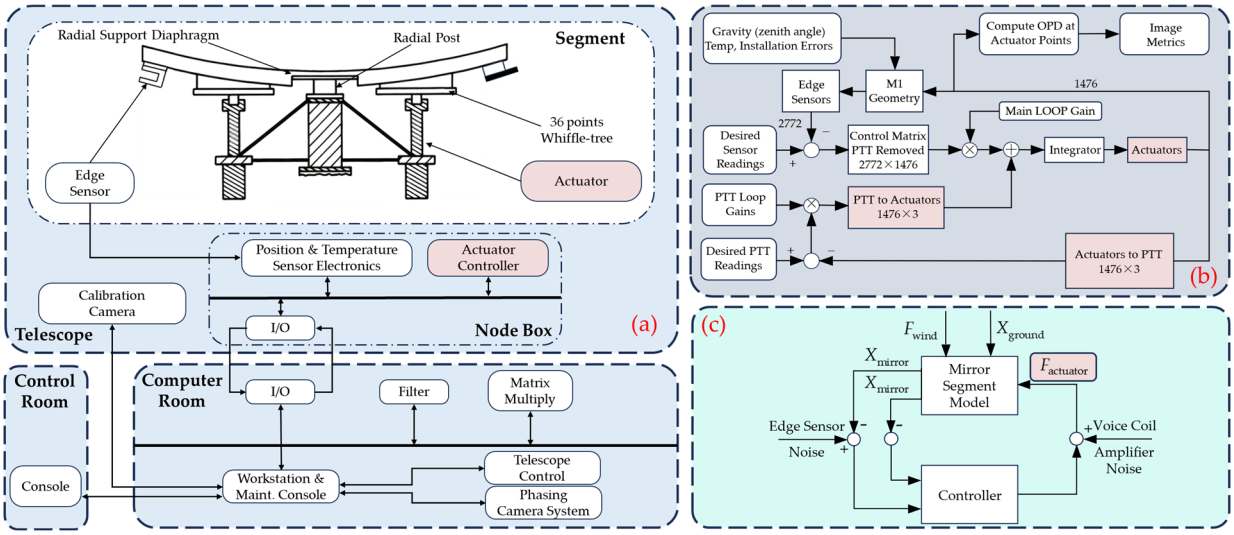

Figure 7. (**a**) The primary mirror support system of Keck. It also shows a simplified electronic/mechanical view of the active control system, depicting the basic operational logic from the initial control strategy to the final mechanical adjustment of the segments [73]; (**b**) Control structure of active maintenance system of segmented mirror in TMT [74]; (**c**) ELT control overall control system [23].

TMT [74–79]

To ensure sufficient control bandwidth for wind-load mitigation, TMT developed the Alignment and Phasing System (APS) and proposed a projection-based alignment strategy that reduces the effective alignment complexity by approximately a factor of 30 without significant information loss. The active control architecture (see Figure 7b) adopts a hierarchical structure consisting of an upper loop using 2772 differential capacitive edge sensors to correct segment misalignments, with reference states recalibrated via APS every 2–4 weeks, and a lower loop driving 1476 VCAs, three per segment, to compensate global piston–tip–tilt errors of the primary mirror.

To mitigate CSI, TMT employs a modal dimension-reduction approach by projecting mirror dynamics onto low-order Zernike modes, enabling robust control design focused on critical structural dynamics. This strategy effectively suppresses structural resonances near 30 Hz and reduces the control design iteration cycle by approximately two orders of magnitude.

ELT [6,80]

For the ELT, a modal analysis-based control framework predicts segment modal responses and decomposes the IM between 2394 actuators and 4608 ES using SVD. By regulating dominant structural modes and iteratively driving the system toward predefined reference states, the closed-loop controller effectively suppresses wind-induced vibrations, structural oscillations, and sensor noise under coupled structural dynamics (see Figure 7c), achieving robust disturbance rejection (see Section 4).

Seimei [31,81]

The 3.8-m Seimei Telescope is the first to adopt a petal-type segmented mirror design, with a total moving mass of 18 tons, less than half that of the 3.5-m ARC telescope. Its segmented mirror control system combines a centralized control system (CCS) and a distributed control system (DCS). The CCS reconstructs the global mirror state from system-wide measurements to provide overall feedback, while the DCS independently regulates segment piston and tilt motions based on local edge-sensor data. Besides the PCS,

laser interferometry is incorporated to improve piston error sensing, particularly under atmospheric turbulence. This lightweight control architecture relies on a high-precision sensor network (ES and WFS), to ensure stability and robustness.

3.2.2. Space-Based Telescope

Compared to ground-based telescopes, space-based segmented telescopes benefit from significantly reduced gravitational and atmospheric turbulence effects while avoiding geographical constraints [82]. Figure 8a illustrates the main technical approaches. Their control systems integrate real-time wavefront sensing with actuators for segment position and surface adjustment, enabling precise co-phasing under micro-vibrations and dynamic space environmental variations. Notable examples include the Segmented Mirror Telescope (SMT) [83,84], the JWST [35] and Large UV/Optical/IR Surveyor (LUVOIR) [85,86]. LUVOIR's steady-state observation control architecture employs noncontact interfaces and multistage control loops within the Vibration Isolation and Precision Pointing System (VIPPS), ensuring high-precision pointing stability. The framework features three hierarchically coordinated loops:

- an innermost loop for line-of-sight error control and estimation;
- an intermediate loop for payload attitude control;
- an outer loop for relative motion between payload and spacecraft.

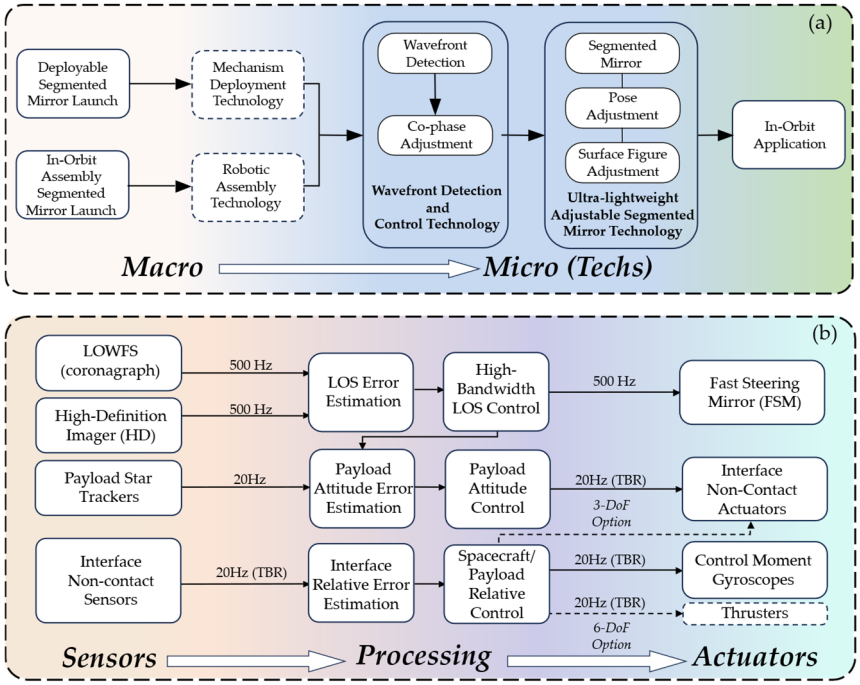

Figure 8. (**a**) Technical approaches for space-based segmented telescopes. Macro-level deployment and robotic assembly technologies overcome fairing constraints and enable larger apertures; micro-level wavefront control and ultra-light adjustable mirrors ensure on-orbit alignment and stable imaging [87–89]; (**b**) LUVOIR steady-state observation control architecture [85].

Using actuators such as fast steering mirrors, VIPPS noncontact actuators, and control moment gyroscopes, this architecture effectively isolates satellite disturbances and achieves stringent dynamic stability requirements.

In summary, this section provides an overview of coordinated control strategies for both single-segment dual-stage actuators and system-level control of segmented mirrors. Decoupled actuators achieve coarse and fine mechanical separation through coarse transmission coupling and a "rise–overshoot/fall–undershoot" strategy, while exploiting the

periodic (sinusoidal) characteristics of eccentric shafts to dynamically compensate for small vibrations/backlash. Dual-drive actuators achieve control-level decoupling using a "sequential closed-loop" approach. The faster VCM continuously counters high-frequency disturbances with dynamic F_{VC}, while the DC motor handles large-stroke adjustments at a slower pace, reducing settling time and allowing the VCM to focus on compensation. The introduction of a "deadband threshold" as an entry point for "the force-feedback" strategy effectively links the coarse and fine stages.

At the system level, ground-based telescopes primarily address modal responses induced by wind loads and ground vibrations. The TMT employs a Zernike-based dimension reduction strategy to simplify the computation of high-dimensional IM, which is essential for generating accurate y_{ref}. Space-based systems benefit from the low-gravity and low-turbulence environment, allowing them to focus on high-bandwidth dynamic control. LUVOIR, for example, uses the VIPPS to mitigate discrete vibrations induced by primary mirror structural modes, achieving picometer-level co-phasing stability. Future segmented mirror systems will build upon these experiences, exploring more efficient and robust hierarchical control architectures and advanced modal decoupling strategies for increasingly large and complex segmented mirrors [52,90–93].

4. Integrated Vibration Isolation Methods for Actuators

Dual-stage actuator based on VCM inherently provide a certain degree of vibration suppression due to their "soft" characteristics and relatively high bandwidth. Their dominant resonance, typically around 10 Hz, lies within the bandwidth of its conventional position control loops. As a result, standard position controllers such as PID naturally introduce effective damping when stabilizing the system, thereby attenuating resonant vibrations.

As discussed earlier, "hard" PZT actuators, which have also been considered for the ELT, offer high passive stiffness in open-loop operation, making them well suited for resisting static loads. In such designs, an additional damping loop is introduced to provide "active damping", suppressing structural resonances (typically in the 40–50 Hz range) above the achievable position control bandwidth (~10 Hz) [42]. This separation of vibration suppression and position regulation simplifies the design of the position loop and facilitates high-precision tracking performance. Beyond the approaches discussed in Section 2.2, a variety of damping-based vibration isolation strategies have been explored in actuator design, which constitute the main focus of this section.

4.1. Damping-Based Vibration Suppression Methods

4.1.1. ELT "Hard" PACT Active Damping [42,43,45]

Although the VCAs are capable of suppressing high-frequency disturbances, its inherently low passive stiffness leads to residual low- and mid-frequency disturbances, as well as amplified high-frequency coil noise (see Figure 7c). These effects can be addressed using targeted control strategies: low- and mid-frequency disturbances are suppressed by integrators and high-bandwidth filters; high-frequency noise is attenuated using low-pass filters.

PZT actuators exhibit the opposite behavior: they possess high passive stiffness even in open-loop operation. However, the position controller has limited authority over high-frequency modes outside its bandwidth, and these sharp resonance peaks persist even when the position loop is disabled. If not sufficiently damped, environmental excitations with nearby frequencies, such as those induced by cooling systems or drive motors, can trigger strong resonances of the actuator–mirror assembly. This not only leads to a severe

degradation in positioning accuracy but also transmits significant vibration to the mirror surface, directly impairing the imaging performance of the telescope.

Therefore, to maximally suppress the dominant resonance modes of the ELT primary mirror (PTT), four key requirements are imposed:

- Sufficient dynamic stiffness was provided for wind-disturbance rejection;
- Adequate closed-loop bandwidth was ensured for M1 primary-mirror control;
- The impact of vibration transmission was restricted;
- Uniform controllers across all segments.

Rigid actuators inherently satisfy the first requirement. The others consider a conventional notch filter and three active damping methods, respectively, as summarized in the Table 4. Therefore, for the ELT M1 segment actuators, the PPF strategy was selected as the preferred solution.

Table 4. Comparison between notch filtering and active damping methods.

Method	Principle	Key Sensor	Pros	Cons
Notch Filter	Creates a "notch" in the control signal at the resonance frequency	(Model-based)	Simple concept	Does not reduce vibration transmission to the segment; Not robust to resonance frequency changes; Impractical to tune for 2394 actuators
Acceleration Feedback (AF)	Uses an accelerometer to measure vibration; feedback force is proportional to velocity	Accelerometer (Additional)	Effective damping	Adds cost, cabling, and failure points; Noisy low-frequency signal requires filtering; Obsolescence management
Force Feedback (FF)	Uses a force washer to measure interface force; feedback is its integral	Force Sensor (Additional)	Best damping performance; Excellent stability (collocation)	Highest complexity/cost; Difficult integration into load path; Sensor must survive extreme loads
Positive Position Feedback (PPF)	Feeds back the position signal through a 2nd-order filter tuned to the resonance	Position Encoder (Existing)	No additional sensors; Adds high-frequency roll-off; Same parameters for all actuators (robust); Low cost, high reliability	Not intuitive (positive feedback);

Figure 9 shows the ELT PPF control architecture. The inner loop is a PPF damping loop that shares the position sensor with the outer position controller C_{pos}. When the system vibrates near a resonance, the PPF filter C_{damp} is tuned to the corresponding resonance frequency and detects the oscillatory component in the position signal. This component is amplified and fed back to generate a force with opposite phase, thereby increasing the effective damping of the mode. This inner-loop conditioning suppresses the resonance

without additional hardware, which reduces lifecycle cost and simplifies obsolescence management over the telescope's 30-year lifetime. An outer PID position loop is then wrapped around the damped plant; because the inner loop has "softened" the system and attenuated the resonance, the C_{pos} design is simpler, more robust, and easier to tune for high-precision tracking. Testing demonstrated a substantial reduction in segment vibration within the 40–50 Hz band (tilt RMS), accompanied by a noticeable decrease in accumulated encoder error. Additionally, this architecture also integrates multistage filtering and gain adjustment, including notch, low-pass, and IIR filters, to smooth position signals and suppress noise.

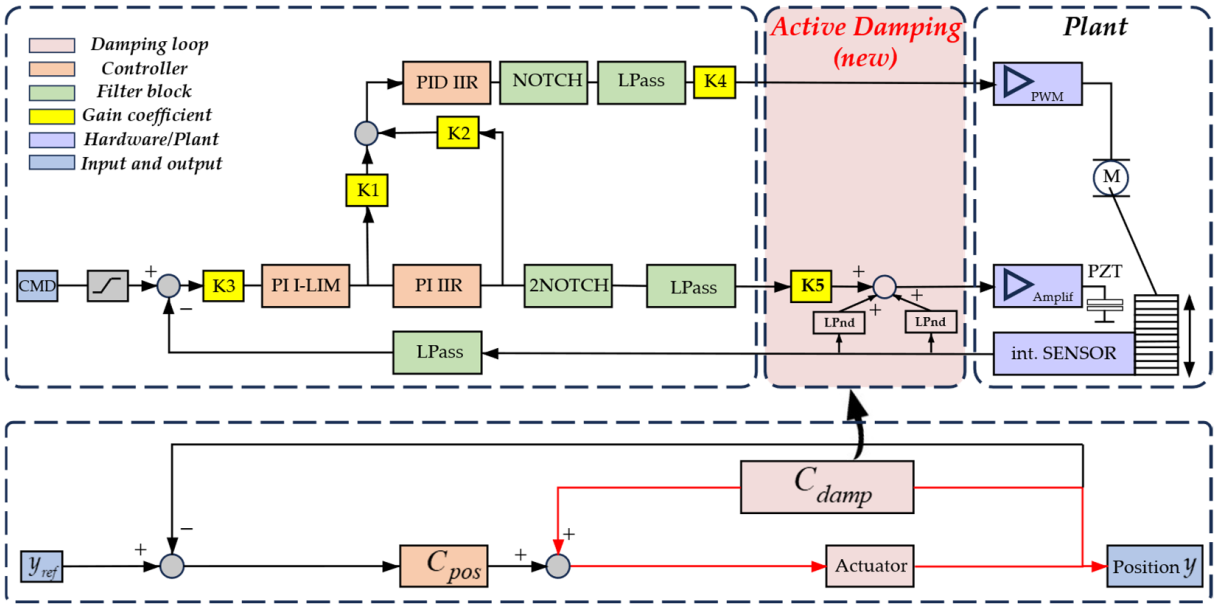

Figure 9. Control block diagram of ELT using active damping: The outer position loop controller C_{pos} (PID) is responsible for precise positioning. The inner loop is the newly added PPF damping loop, which shares the position sensor with the outer loop and is responsible for increasing system damping to suppress resonances outside the position control bandwidth [42,43].

4.1.2. Other Damping-Based Approaches

To enhance observational performance under extreme conditions, large-scale optical telescopes, such as the airborne SOFIA [94–97], have incorporated vibration isolation structures, such as tuned mass dampers (TMD) and reaction-mass actuators (RMA). These devices passively or actively generate damping forces tailored to specific modal disturbances. By integrating auxiliary mass-spring systems at multiple telescope locations, they enable multistage vibration isolation, coupling with target vibration modes to thermally dissipate energy, effectively suppressing vibrations across frequency ranges and achieving 0.5 arcseconds RMS LOS pointing stability. Yao et al. [98] employed inertial PZT actuators to mitigate cantilever vibrations through out-of-phase inertial forces, achieving amplitude reductions of approximately 53.2%, 46%, and 50.4% at excitation frequencies of 50, 75, and 100 Hz. Zhang [99] developed active isolation units driven by VCMs, leveraging their rapid response, long stroke, and zero stiffness to create dynamic absorbers with anti-resonant frequencies; under a ground vibration velocity of 7 mm/s, the load vibration amplitude decreased from 4 mm/s to 1.3 mm/s, a 67.5% reduction. Similarly, Qin [100] applied AF and FF active damping controllers in a VCM-based TMD, yielding roughly 50% attenuation of test-point acceleration, with FFT analysis indicating the resonance peak was suppressed to about one-fifth of its original value. Additionally, Jiang et al. [101] investigated magnetorheological fluids as smart materials for active isolation, demonstrating broadband

vibration suppression with efficiency exceeding 90% in both vertical and lateral directions in three-axis random vibration tests. The Gemini Planet Imager [97] employs an undamped tunable vibration absorber (TVA) on its cryocoolers, which constitute the dominant vibration source, to mitigate single-frequency disturbances at 60 Hz, as the undamped design provides maximum theoretical suppression efficiency for a well-defined, stable frequency.

Unlike feedback-based active damping, vibration suppression for servo system start–stop shocks can be achieved using feedforward strategies. Techniques such as velocity trajectory planning [102–105] and input shaping [106–108] modify control commands to reduce excitation without altering the servo mechanics.

4.2. Modal and Vibration-Sensitivity Analysis

Regardless of whether feedback-based active damping or open-loop feedforward strategies are employed, "active" vibration suppression fundamentally refers to purposeful mitigation of specific disturbances.

Vibration-sensitivity analysis is crucial for understanding how vibrations propagate to wavefront errors and for guiding effective suppression methods. Vibration measurement platforms can rapidly measure frequency responses of segment errors, and IFFT techniques allow derivation of corresponding time-domain responses, reducing the complexity of multi-segment, multi-node systems [13,79]. Domestically, Zhou et al. at CIOMP have developed force-measurement platforms to detect complex coupled disturbances in large-scale systems. These platforms integrate piezoelectric and strain-sensing elements, enabling high-precision measurements under dynamic coupling and high base frequencies, while intelligent algorithms provide parameter optimization and multi-sensor fault tolerance [109–117]. Such approaches offer valuable insights for the integrated design of vibration-suppressed, high-precision segmented mirror systems.

During the ELT actuator design phase, open-loop power spectral-density analysis identified disturbance frequencies with significant impact on co-phasing accuracy [43]. To quantify the influence of vibration sources and refine actuator inputs for vibration mitigation, Sedghi et al. [80] conducted a vibration -sensitivity analysis by integrating finite-element, control, and optical models of the ELT and its M1 primary mirror. Their analysis involved the following steps:

- Vibration sources (e.g., dome environment, M2–M5 systems, instruments, and electronics) were identified using finite-element modeling;
- Frequency responses of each vibration source to segment PTT motions were calculated;
- The frequency-response matrix from vibration inputs to segment PTT motions was derived (see [80] for details), with its size depending on the number of actuators (for ELT, this number is large).

The finite-element model enabled fast computation of the vibration-to-PTT frequency responses. However, large-scale matrix inversion requires significant computational resources. Once precomputed, these frequency responses support downstream processes like wavefront-error calculation and mirror-mode transformation. Using IFFT, time-domain PTT responses were derived, validating the frequency-response analysis.

The analysis also quantified the magnitude and phase of the responses, identifying the most vibration-sensitive source locations and frequencies. Time-domain simulations confirmed the accuracy of the frequency-response analysis. Based on these findings, strategies were developed to mitigate vibration effects, including structural optimization, high-bandwidth PTT actuators, servo-control improvements, and active vibration-control algorithms (e.g., active damping) to reduce wavefront errors. This vibration-sensitivity analysis provides valuable insights for targeting vibration suppression methods to improve telescope imaging quality.

5. Summary and Outlook

As key execution components of AO, dual-stage actuators have been increasingly adopted for mirror stabilization in segmented mirror systems. Compared with traditional scaled single-stage actuators, they offer improved overall dynamic performance and a more balanced solution to the trade-off between large stroke and high precision. Although dual-stage architectures inherently introduce decoupling challenges between coarse and fine stages, decoupled actuators and dual-drive actuators address potential overshoot and oscillation issues through mechanical decoupling strategies and sequential closed-loop control strategies, respectively. VCAs, benefiting from the high bandwidth, fast response, and ease of control of VCM, are well suited for compensating high-frequency segment vibrations. In contrast, PZT actuators [34,42] are also attractive candidates. Their high passive stiffness provides superior resistance to quasi-static loads, while active damping techniques effectively suppress resonances beyond the position-control bandwidth. These active approaches can be optimized to target specific disturbance frequencies or sources, dissipating vibrational energy in a directed manner. Force-measurement platforms developed by Zhou et al. [109–117], together with the disturbance-sensitivity analysis conducted for the ELT, further identify dominant vibration modes and disturbance paths, providing critical guidance for improving vibration-suppression efficiency.

At the single-actuator level, the role of ES was discussed in detail. By measuring relative displacements between adjacent segments and enabling degree-of-freedom decoupling through appropriate reconstruction algorithms, ESs provide reference position commands to actuators. The IM links sensor measurements and actuator commands, while high-precision feedback devices, such as grating encoders, ensure positioning accuracy. At the system level, challenges shift toward the computation of high-dimensional IM and the treatment of globally weakly observable modes, such as clocking or torsional modes. Ground-based segmented telescopes primarily emphasize real-time multimodal decoupling and disturbance rejection under environmental excitations, whereas space-based systems prioritize non-contact vibration isolation and hierarchically nested control loops to achieve ultra-stable pointing and wavefront control.

Despite these advances, dual-stage actuators still face challenges in macro–micro coordination, nonlinear dynamics, and scalability in load capacity due to complex performance trade-offs. To address these, future research will focus on several key directions [118]:

- Cross-scale collaborative control strategies. Hybrid strategies, such as combining model predictive control with sliding-mode algorithms, are expected to achieve sub-nanometer wavefront error control while extending high-frequency suppression beyond 150 Hz, essential for operation in more dynamic environments;
- Smart materials and structural innovation. Lightweight mirror segments, such as those made from SiC, will reduce the total moving mass. This directly enables faster actuator response, improves pointing agility, and reduces the power required for positioning. Concurrently, active vibration isolation will evolve by integrating smart materials into actuator and support structures. Magnetorheological fluids [101], for instance, can be used in adaptive dampers whose stiffness and damping properties can be tuned in real-time via magnetic fields, offering broadband vibration suppression tailored to changing disturbance spectra. Similarly, the use of piezoelectric materials not just as PZT but also as embedded sensors for health monitoring and active damping will lead to more compact and multifunctional “smart” actuator units.
- AI-based adaptive parameter optimization. AI or deep learning will revolutionize system calibration and maintenance. AI-based adaptive parameter optimization aims to reduce initial calibration time from weeks to under 24 h and enable continuous performance adaptation. Furthermore, AI-facilitated co-design will optimize the

interplay between mechanical architecture, control strategies, and optical performance from the outset.

Ultimately, deeper integration of mechanical design, intelligent control algorithms, and system-level co-design is anticipated to enable further breakthroughs in astronomical observation capabilities.

Author Contributions: Methodology, W.W. and Q.A.; validation, W.W.; writing—original draft: W.W.; writing—editing: W.W. and Q.A.; project administration, X.W.; funding acquisition, X.W. and Q.A. All authors have read and agreed to the published version of the manuscript.

Funding: This work was supported by the National Natural Science Foundation of China (Grant No. 12133009), the National Natural Science Foundation of China (Grant No. 12373090), the Jilin Provincial Department of Science and Technology (Grant No. 20250101025JJ), and the Science and Technology Application Promotion Fund (Grant No. 145XXX050532000X).

Data Availability Statement: The original contributions presented in this study are included in the article. Further inquiries can be directed to the corresponding authors.

Acknowledgments: I would like to express my sincere gratitude to my advisors, An and Wu, for their dedicated guidance and support. Their valuable advice and patient assistance were instrumental in the completion of this review.

Conflicts of Interest: The authors declare no conflicts of interest.

Abbreviations

The following abbreviations are used in this manuscript:

AO	active optics
TMT	Thirty Meter Telescope
ELT	extremely large telescope
PTT	piston–tip–tilt
VCA	voice-coil actuator
VCM	voice-coil motor
HDMA	hydraulic micro-displacement amplifier
ES	edge sensor
WFS	wavefront sensor
PPF	positive position feedback
AF	acceleration feedback
FF	force feedback
PID	proportional-integral-derivative
SVD	singular value decomposition
IM	interaction matrix
CSI	control–structure interaction
GTC	Gran Telescopio Canarias
HET	Hobby–Eberly Telescope
SALT	Southern African Large Telescope
LAMOST	Large Sky Area Multi-Object Fiber Spectroscopic Telescope
APS	alignment and phasing system
PCS	Phasing Camera System
CCS	centralized control system
DCS	distributed control system
JWST	James Webb Space Telescope
LUVOIR	Large UV/Optical/IR Surveyor
SMT	Segmented Mirror Telescope
VIPPS	Vibration Isolation and Precision Pointing System
SOFIA	Stratospheric Observatory for Infrared Astronomy

LOS	line-of-sight
LGS	laser-guide stars
PACT	position actuator
TMD	tuned mass damper
RMA	reaction-mass actuators
TVA	tunable vibration absorber

References

1. Li, X.T.; Cen, Z.F. *Geometrical Optics, Aberrations and Optical Design*; Zhejiang University Press: Hangzhou, China, 2007; pp. 299–300.
2. Yu, W.H.; Li, B.; Chen, M.; Xian, H. Experimental investigation on active control of segmented primary mirror. *Laser Optoelectron. Prog.* **2017**, *54*, 222–229. [CrossRef]
3. Sanders, G. Thirty Meter telescope project update. In *Proceedings Volume 8444, Ground-Based and Airborne Telescopes IV*; SPIE: Bellingham, WA, USA, 2014; pp. 9145–9148.
4. Argomedo, J.; Kornweibel, N.; Grudzien, T.; Dimmler, M.; Andolfato, L.; Barriga, P. Prototyping the E-ELT M1 local control system communication infrastructure. In Proceedings of the Software and Cyberinfrastructure for Astronomy IV, Edinburgh, UK, 26 June–1 July 2016; pp. 635–644. [CrossRef]
5. Thirty Meter Telescope (TMT). Available online: http://www.tmt.org (accessed on 10 May 2025).
6. European Extremely Large Telescope (E-ELT). Available online: https://elt.eso.org/ (accessed on 10 May 2025).
7. Cho, M.K.; Stepp, L.; Kim, S. *Wind Buffeting Effects on the Gemini 8-m Primary Mirrors*; SPIE: Bellingham, WA, USA, 2001; Volume 4444, pp. 302–314. [CrossRef]
8. Cao, Y.Y. Research on wind disturbance analysis and suppression for the large ground-based optical telescope. Ph.D. Thesis, University of Chinese Academy of Sciences, Changchun, China, 2023.
9. Liao, H.Y. *Analysis of Influence of Wind Load on Tracking Error of Large-Aperture Optical Telescope*; Graduate University of Chinese Academy of Sciences: Chengdu, China, 2014.
10. Thompson, P.; MacMynowski, D.; Sirota, M. *Analysis of the TMT Mount Control System*; SPIE: Bellingham, WA, USA, 2008; Volume 7012, pp. 70121P-1–70121P-14. [CrossRef]
11. Neill, D.; Sebag, J.; Warner, M.; Krabbendam, V. *Wind Induced Image Degradation (Jitter) of the LSST Telescope*; SPIE: Bellingham, WA, USA, 2008; Volume 7012, pp. 70120W-1–70120W-11. [CrossRef]
12. Qi, A. Overview of wind load analysis of large telescope. *J. Mech. Electr. Eng.* **2015**, *1983*, 1649–1652. [CrossRef]
13. Yu, J.-H.; Xue, S.; Luan, T.; Wang, L.-Y.; Lian, P.-Y.; Yan, Y.-F.; Kong, D.-Q.; Zhao, W.-L.; Xu, Q.; Wang, C.-S. Large Telescope Wind Load Estimation with Gradient Segments Superposition and its Servo Control. *Res. Astron. Astrophys.* **2023**, *23*, 095008. [CrossRef]
14. Rippa, M.; Bonnet, H.; Hayward, T.; Trujillo, C.; Cavedoni, C.; Cumming, T.; Yamasaki, C.; Masuda, N.; Bagano, C.; Hardash, S. *Rejecting Harmonic Vibrations at Gemini with Real-Time Vibration Tracking*; SPIE: Bellingham, WA, USA, 2016; Volume 9913, pp. 99132M-1–99132M-13. [CrossRef]
15. Shi, J.W. Research on position actuators in large-aperture segmented mirror telescope. Ph.D. Thesis, Nanjing University of Posts and Telecommunications, Nanjing, China, 2021. [CrossRef]
16. Huo, Y.L.; Yang, F.; Wang, F.G. Overview of key technologies for segmented mirrors of large-aperture optical telescopes. *Chin. Opt.* **2022**, *15*, 973–982. [CrossRef]
17. MacMartin, D.G.; Roberts, L.C.; Shelton, J.C.; Chanan, G.A.; Bonnet, H. In-plane effects on segmented-mirror control. *Appl. Opt.* **2012**, *51*, 1929–1938. [CrossRef]
18. Glaese, R.; Sheehan, M. *Vibration Mitigation for Wind-Induced Jitter for the Giant Magellan Telescope*; SPIE: Bellingham, WA, USA, 2012; Volume 8444, pp. 84440V-1–84440V-15. [CrossRef]
19. Jiménez, A.; Morante, E.; Viera, T.; Núñez, M.; Reyes, M. *Design of a Prototype Position Actuator for the Primary Mirror Segments of the European Extremely Large Telescope*; SPIE: Bellingham, WA, USA, 2010; Volume 7733, p. 773354. [CrossRef]
20. Adams, D.; Vaccarella, A.; Schofield, W.; Sharp, R.; Gilbert, J.; Gausachs, G. *Vibration Measurement and Mount Design for Cryocoolers on GMT and Large Telescopes*; SPIE: Bellingham, WA, USA, 2020; Volume 11203. [CrossRef]
21. Gillingham, P. *Operational Performance of the Keck 10-m Telescope*; SPIE: Bellingham, WA, USA, 1997; Volume 2871, pp. 2–9. [CrossRef]
22. Meng, J.; Franck, J.; Gabor, G.; Jared, R.; Minor, R.; Schaefer, B. *Position Actuators for the Primary Mirror of the W. M. Keck Telescope*; SPIE: Bellingham, WA, USA, 1990; Volume 1236, pp. 1018–1022. [CrossRef]
23. Cohen, R.; Andreae, S.; Biocca, A.; Jared, R.; Llacer, J.; Meng, J.; Minor, R.; Orayani, M.W.M. *Keck Telescope Segmented Primary Mirror Active Control System Software*; SPIE: Bellingham, WA, USA, 1990; Volume 1236, pp. 996–1008. [CrossRef]

24. Kamphues, F.; Nijenhuis, J.; den Breeje, R.; van den Dool, T.; Ponsioen, J. *PACT: The Actuator to Support the Primary Mirror of the ELT*; SPIE: Bellingham, WA, USA, 2008; Volume 7018, pp. 70180Z-1–70180Z-10. [CrossRef]
25. Mast, T.; MacMartin, D.; Nelson, J.; Chanan, G. Active control issues for the California Extremely Large Telescope. In *AIAA Guidance, Navigation, and Control Conference and Exhibit*; American Institute of Aeronautics and Astronautics (AIAA): Reston, VA, USA, 2001; pp. 2001–4035. [CrossRef]
26. Lefort, B.; Castro, J. *The GTC Primary Mirror Control System*; SPIE: Bellingham, WA, USA, 2008; Volume 7019, p. 70190I. [CrossRef]
27. Yang, D.H.; Qi, Y.J.; Zhu, Z.D.; Jiang, F.H.; Chen, K.X.; Zhang, R. Design and test of the active micro-motion mechanism for optical mirror segement. *Opt. Precis. Eng.* **2005**, *13*, 191–197. [CrossRef]
28. Krabbendam, V.; Sebring, T.; Ray, F.; Fowler, J. *Development and Performance of Hobby-Eberly Telescope 11-m Segmented Mirror*; SPIE: Bellingham, WA, USA, 1998; Volume 3352, pp. 436–445. [CrossRef]
29. Swiegers, J.; Gajjar, H. *Completion of the Southern African Large Telescope (SALT) Primary Mirror System*; SPIE: Bellingham, WA, USA, 2004; Volume 5489, pp. 881–891. [CrossRef]
30. Yang, D.; Jiang, F. *Support System Design of the Sub-Mirror Cell of the LAMOST Schmidt Plate*; SPIE: Bellingham, WA, USA, 2006; Volume 6273, p. 62731H. [CrossRef]
31. Kurita, M.; Kino, M.; Iwamuro, F.; Ohta, K.; Nogami, D.; Izumiura, H.; Yoshida, M.; Matsubayashi, K.; Kuroda, D.; Nakatani, Y.; et al. The Seimei telescope project and technical developments. *Publ. Astron. Soc. Jpn.* **2020**, *46*, 48. [CrossRef]
32. Zhang, Z.M.; Wang, Z.L.; Yang, D.H.; Wu, C.C.; Jin, Z.Y. Design and experimental validation of stepper motor-based displacement actuators. *Astron. Res. Technol.* **2019**, *16*, 329–334.
33. Shuai, Y.L.; Niu, D.S.; Wang, H.; Pan, C. Research on Micro-displacement Actuator for High Precision Mirror Position Control. *Astron. Res. Technol.* **2023**, *20*, 250–257.
34. Zhan, W.; Liu, T.; Chen, S.; Kai, L.; Liu, J.K.; Liu, Y.X.; Chen, W.S. A Piezo-Hydraulic actuator design supporting fast steering mirror. *Int. J. Mech. Sci.* **2025**, *294*, 110214. [CrossRef]
35. Mark, C. *Status of the James Webb Space Telescope (JWST)*; SPIE: Bellingham, WA, USA, 2008; Volume 7010, p. 70100L. [CrossRef]
36. Streetman, S.; Kingsbury, L. *Cryogenic Nano-Positioner Development and Test for Space Applications*; SPIE: Bellingham, WA, USA, 2003; Volume 4850, pp. 274–285. [CrossRef]
37. Barto, A.; Acton, D.; Finley, P.; Gallagher, B.; Hardy, B.; Knight, J.; Lightsey, P. *Actuator Usage and Fault Tolerance of the James Webb Space Telescope Optical Element Mirror Actuators*; SPIE: Bellingham, WA, USA, 2012; Volume 8442, p. 84422I. [CrossRef]
38. Warden, R.M. Cryogenic nano-actuator for JWST. In *Proceedings of 38th Aerospace Mechanisms Symposium*; Langley Research Center: Hampton, VA, USA, 2006; pp. 239–252.
39. Wu, S.H.; Dong, J.H.; Yu, F.N.; Xu, F.Y. Design and Research of Active Support Actuator for Large Diameter Space Assembly Telescope. *Mach. Des. Manuf.* **2022**, *2*, 135–138.
40. Carter, C.; Colavita, M.M. *TMT Primary Mirror Segment Actuators: From Prototyping to Production*; SPIE: Bellingham, WA, USA, 2024; Volume 13094, p. 1296909. [CrossRef]
41. Lorell, K.R.; Aubrun, J.N.; Clappier, R.R.; Miller, S.W.; Sirota, M. *Design of a Prototype Primary Mirror Segment Positioning Actuator for the Thirty Meter Telescope*; SPIE: Bellingham, WA, USA, 2006; Volume 6267, pp. 62672T-1–62672T-11. [CrossRef]
42. Sedghi, B.; Dimmler, M.; Müller, M.; Kornweibel, N. *Improving E-ELT M1 Prototype Hard Position Actuators with Active Damping*; SPIE: Bellingham, WA, USA, 2016; Volume 9906, pp. 99062W-1–99062W-12. [CrossRef]
43. Witvoet, G.; Breeje, R.D.; Nijenhuis, J.; Hazelebach, R.; Doelman, N. Dynamic analysis and control of mirror segment actuators for the European Extremely Large Telescope. *J. Astron. Telesc. Instrum. Syst.* **2015**, *1*, 019003. [CrossRef]
44. Witvoet, G.; Breeje, R.D.; Nijenhuis, J.; Hazelebach, R.; Doelman, N. *High Performance Control of Mirror Segment Actuators for the European Extremely Large Telescope*; SPIE: Bellingham, WA, USA, 2014; Volume 9145, pp. 91451S-1–91451S-14. [CrossRef]
45. Pettazzi, L.; Sedghi, B.; Reinacher, A.; Dimmler, M.; Barriga, P.; Zuluaga Ramirez, P.; Cayrel, M.; Dietzel, O.; Ebert, M.; Maier, T. Results of the ELT M1 position actuators validation campaign. In *Advances in Optical and Mechanical Technologies for Telescopes and Instrumentation IV*; SPIE: Bellingham, WA, USA, 2020; Volume 11451, pp. 378–392. [CrossRef]
46. Deshmukh, P.G.; Mandal, A.; Parihar, P.S.; Nayak, D.; Mishra, D.S. Design, development, and validation of a segment support actuator for the prototype segmented mirror telescope. *J. Astron. Telesc. Instrum. Syst.* **2018**, *4*, 014005. [CrossRef]
47. Deshmukh, P.; Parihar, P.; Mishra, D.S.; Prakash, A.; Kemkar, P.M.M. *A Soft Actuator for Prototype Segmented Mirror Telescope*; SPIE: Bellingham, WA, USA, 2016; Volume 9912, p. 991207. [CrossRef]
48. Liu, Y.S. Research on the Technologies of Micro-Displacement Actuator for Large Aperture Segmented Optical/Infrared Telescope. Ph.D. Thesis, Changchun Institute of Optics, Fine Mechanics and Physics, Chinese Academy of Sciences, Changchun, China, 2021.
49. Monnier, J.D. Optical interferometry in astronomy. *Rep. Prog. Phys.* **2003**, *66*, 789. [CrossRef]
50. Eisenhauer, F.; Monnier, J.D.; Pfuhl, O. Advances in optical/infrared interferometry. *Annu. Rev. Astron. Astrophys.* **2023**, *61*, 237–285. [CrossRef]
51. Aubrun, J.N.; Lorell, K.R.; Havas, T.W.; Henninger, W.C. Performance analysis of the segment alignment control system for the ten-meter telescope. *Automatica* **1988**, *24*, 437–453. [CrossRef]

52. Chiozzi, G.; Andolfato, L.; Argomedo, J.; Benes, N.; Cano, C.D.; Urrutia, A.H.; Kornweibel, N.; Lampater, U.; Pellegrin, F.; Schilling, M. The ELT Control System: Recent Developments. In Proceedings of the ICALEPCS2021, Shanghai, China, 14–22 October 2021.
53. Lorell, R.K.; Aubrun, J.; Perez, O.E.; Reshatoff, J.P., Jr.; Zacharie, F. *D Test and Performance Evaluation of the Gemini Secondary Mirror Chopper and Position Control System*; SPIE: Bellingham, WA, USA, 1998; Volume 3351, pp. 102–115. [CrossRef]
54. Yin, J.; Zhu, S.Y.; Ni, J.J.; Chen, X.T.; Feng, Z.H. Method for LAMOST cofocus maintenance based on an Eddy current edge sensor. *Appl. Opt.* **2024**, *63*, 4745–4753. [CrossRef]
55. Yin, J.; Zhao, G.F.; Feng, Z.H.; Ni, J.J. A novel dual-differential edge sensor based on the eddy current effect. *IEEE Sens. J.* **2023**, *23*, 6129–6138. [CrossRef]
56. Acton, D.S.; Bouchez, A. Phasing Metrology System for the GMT. In *Ground-Based and Airborne Telescopes IV*; SPIE: Bellingham, WA, USA, 2012; Volume 8444, pp. 755–764. [CrossRef]
57. Chanan, G.; Troy, M.; Dekens, F.; Michaels, S.; Nelson, J.; Mast, T.; Kirkman, D. Phasing the mirror segments of the Keck telescopes: The broadband phasing algorithm. *Appl. Opt.* **1998**, *37*, 140–155. [CrossRef]
58. Chanan, G.; Ohara, C.; Troy, M. Phasing the mirror segments of the Keck telescopes II: The narrow-band phasing algorithm. *Appl. Opt.* **2000**, *39*, 4706–4714. [CrossRef]
59. Shi, F.; Chanan, G.; Ohara, C.; Troy, M.; Redding, C.D. Experimental verification of dispersed fringe sensing as a segment phasing technique using the Keck telescope. *Appl. Opt.* **2004**, *43*, 4474–4481. [CrossRef] [PubMed]
60. Esposito, S.; Pinna, E.; Puglisi, A.; Tozzi, A.; Stefanini, P. Pyramid sensor for segmented mirror alignment. *Opt. Lett.* **2005**, *30*, 2572–2574. [CrossRef] [PubMed]
61. Hénault, F. Multi-spectral piston sensor for co-phasing giant segmented mirrors and multi-aperture interferometric arrays. *J. Opt. A Pure Appl. Opt.* **2009**, *11*, 125503. [CrossRef]
62. Mazzoleni, R.; Gonté, F.; Surdej, I.; Araujo, C.; Brast, R.; Derie, F.; Duhoux, P.; Dupuy, C.; Frank, C.; Karban, R. Design and performances of the Shack-Hartmann sensor within the Active Phasing Experiment. In *Ground-Based and Airborne Telescopes II*; SPIE: Bellingham, WA, USA, 2008; Volume 7012, pp. 1246–1257. [CrossRef]
63. Lou, J.Z.; Redding, D.C.; Nissen, J.A.; Shelton, A. LUVOIR primary mirror segment alignment control with joint laser metrology and segment edge sensing. In *Space Telescopes and Instrumentation 2018: Optical, Infrared, and Millimeter Wave*; SPIE: Bellingham, WA, USA, 2018; Volume 10698, pp. 1184–1197. [CrossRef]
64. Rakich, A.; Schurter, P.; Conan, R.; Hill, M.J.; Gardiner, M.; Bec, M.; Kuhn, O. Prototyping the GMT telescope metrology system on LBT. In *Ground-Based and Airborne Telescopes VII*; SPIE: Bellingham, WA, USA, 2018; Volume 10700, pp. 548–558. [CrossRef]
65. Zhao, F. Picometer laser metrology for the Space Interferometry Mission (SIM). In *Proceedings of the Conference on Lasers and Electro-Optics; CTuO5*; Optica Publishing Group: Washington, DC, USA, 2004.
66. Wasmeier, M.; Hackl, J.; Leveque, S. Inductive sensors based on embedded coil technology for nanometric inter-segment position sensing of the E-ELT. In *Ground-Based and Airborne Telescopes, V*; SPIE: Bellingham, WA, USA, 2014; Volume 9145, pp. 647–659. [CrossRef]
67. Reinacher, A.; Sedghi, B.; Dimmler, M.; Lampater, U. ELT M1 edge sensors in the figure control loop: Simulations and test results. In *Ground-Based and Airborne Telescopes IX*; SPIE: Bellingham, WA, USA, 2022; Volume 12182, pp. 698–711. [CrossRef]
68. Rozière, D.; Luong, B.; Fuchs, B.; Périn, A.; Néel, C.; Lévèque, S. Inductive edge sensors: An innovative solution for ELT segmented mirror alignment monitoring. In *Ground-Based and Airborne Telescopes II*; SPIE: Bellingham, WA, USA, 2008; Volume 7012, pp. 469–482. [CrossRef]
69. Shelton, C.; Roberts, L.C., Jr. How to calibrate edge sensors on segmented mirror telescopes. In *Ground-Based and Airborne Telescopes IV*; SPIE: Bellingham, WA, USA, 2012; Voluem 8444, pp. 1926–1941. [CrossRef]
70. Mast, T.; Chanan, G.; Nelson, J.; Minor, R.; Jared, R. Edge sensor design for the TMT. In *Ground-Based and Airborne Telescopes*; SPIE: Bellingham, WA, USA, 2006; Volume 6267, pp. 974–988. [CrossRef]
71. Aubrun, J.N.; Lorell, K.R. Segment alignment control system. In *Report of the Asilomar 3 LDR Workshop*; Jet Propulsion Laboratory, California Institute of Technology: Pasadena, CA, USA, 1988.
72. Schoeck, M.; Chanan, G.; Michaels, S.; Troy, M. Thirty Meter Telescope alignment and phasing system risk reduction studies and experiments. In *Ground-Based and Airborne Telescopes, X*; SPIE: Bellingham, WA, USA, 2024; Volume 13094, pp. 971–981. [CrossRef]
73. Jared, R.C.; Arthur, A.A.; Andreae, S.; Biocca, K.A.; Cohen, W.R.; Fuertes, M.J.; Franck, J.; Gabor, G.; Llacer, J.; Mast, S.T. WM Keck Telescope segmented primary mirror active control system. In *Advanced Technology Optical Telescopes IV*; SPIE: Bellingham, WA, USA, 1990; Volume 1236, pp. 996–1008. [CrossRef]
74. MacMynowski, D.; Thompson, P.; Shelton, J.; Roberts, L.; Colavita, M.; Sirota, M. *Control System Modeling for the Thirty Meter Telescope Primary Mirror*; SPIE: Bellingham, WA, USA, 2011; Volume 8336, p. 83360R. [CrossRef]
75. Piatrou, P.; Chanan, G. Projection approach to complexity reduction in tomographic alignment of extremely large telescopes. *Appl. Opt.* **2012**, *51*, 704–712. [CrossRef]

76. Piatrou, P.; Chanan, G. *Overview of the Control Strategies for the TMT Alignment and Phasing System*; SPIE: Bellingham, WA, USA, 2011; Volume 8149, p. 81490A. [CrossRef]
77. Thompson, P.M.; MacMynowski, D.G.; Regehr, M.W.; Colavita, M.M.; Sirota, J.M. Servo design and analysis for the Thirty Meter Telescope primary mirror actuators. In *Ground-Based and Airborne Telescopes III*; SPIE: Bellingham, WA, USA, 2010; Volume 7733, pp. 863–876. [CrossRef]
78. MacMartin, D.G.; Thompson, P.M.; Colavita, M.M.; Sirota, M.J. Dynamic analysis of the actively-controlled segmented mirror of the thirty meter telescope. *IEEE Trans. Control. Syst. Technol.* **2013**, *22*, 58–68. [CrossRef]
79. Eto, Y.; Kato, A.; Horiuchi, T.; Saruta, Y.; Sofuku, S.; Nakaoji, T.; Kawaguchi, N.; Takaki, J.; Horiuchi, Y.; Haruna, M. *Overview of Key Technologies for TMT Telescope Structure*; SPIE: Bellingham, WA, USA, 2016; Volume 9906, p. 99060Y. [CrossRef]
80. Sedghi, B.; Müller, M.; Dimmler, M. *Analyzing the Impact of Vibrations on E-ELT Primary Segmented Mirror*; SPIE: Bellingham, WA, USA, 2016; Volume 9911, pp. 991111-1–991111-11. [CrossRef]
81. Ichiro, J.; Daichi, U.; Masaru, K.; Mikio, K.; Katsuhiko, Y. Structure of distributed control system in Seimei telescope. *SICE J. Control Meas. Syst. Integr.* **2021**, *14*, 111–118. [CrossRef]
82. Lillie, C. *Large Deployable Telescopes for Future Space Observatories*; SPIE: Bellingham, WA, USA, 2005; Volume 5899, p. 58990D. [CrossRef]
83. Allen, M.R.; Kim, J.J.; Agrawal, B.N. Correction of an active space telescope mirror using a deformable mirror in a woofer-tweeter configuration. *J. Astron. Telesc. Instrum. Syst.* **2016**, *2*, 029001. [CrossRef]
84. Watson, J.J. *Correcting Surface Figure Error in Imaging Satellites Using a Deformable Mirror*; Naval Postgraduate School: Monterey, CA, USA, 2013.
85. Sacks, L.; Blaurock, C.; Dewell, L.; Tajdaran, K.; Liu, K.-C.; Collins, C.; West, G.; Ha, K.; Bolcar, M.; Crooke, J.; et al. *Preliminary Jitter Stability Results for the Large UV/Optical/Infrared (LUVOIR) Surveyor Concept Using a Non-Contact Vibration Isolation and Precision Pointing System*; SPIE: Bellingham, WA, USA, 2018; Volume 10698, p. 106980S. [CrossRef]
86. The LUVOIR Team. The LUVOIR mission concept study final report, NASA Technical Memorandum NASA-TM-2019-220246. *arXiv* **2019**, arXiv:1912.06219. [CrossRef]
87. Hu, B.; Li, C.; Xiang, M.; Li, L.L.; Dai, H.B.; Yao, P.; Li, X.Y. Development and prospects of deployable space optical telescope technology. *Infrared Laser Eng.* **2021**, *50*, 347–362. [CrossRef]
88. Wang, K.; Wang, B.J.; Xu, B.Q.; Gao, Y. Key Technology of Opto-mechanical Structure for On-orbit Assembly Space Telescope. *Spacecr. Eng.* **2024**, *33*, 110–117. [CrossRef]
89. Zhao, K.L.; Sun, D.W.; Huang, Q.L.; Tian, G.L.; He, J.P. Research status and development trend of segmented space telescope technology. *Spacecr. Recovery Remote Sens.* **2024**, *45*, 78–89. [CrossRef]
90. Thompson, P.; MacMynowski, D.; Sirota, M. *Control Analysis of the TMT Primary Segment Assembly*; SPIE: Bellingham, WA, USA, 2008; Volume 7012, pp. 70121N-1–70121N-14. [CrossRef]
91. Fan, W.-Q.; Wang, Z.-C.; Chen, B.-G.; Li, H.-W.; Chen, T.; An, Q.-C.; Fan, L. Review of the active control technology of large aperture ground telescopes with segmented mirrors. *Chin. Opt.* **2020**, *13*, 1194–1208. [CrossRef]
92. Sirota, M.J.; Angeli, G.Z.; MacMynowski, D.G.; Mast, T.S.; Nelson, J.E.; Chanan, G.A.; Colavita, M.M.; Lindensmith, C.A.; Shelton, C.; Troy, M.; et al. An overview of the active optics control strategy for the thirty meter telescope. *Sensors* **2011**, *10*, 211–214.
93. Contos, A.; Acton, D.S.; Atcheson, P.; Barto, A.; Lightsey, P.; Shields, D. *Bringing It All Together: A Unique Approach to Requirements for Wavefront Sensing and Control on the James Webb Space Telescope (JWST)*; SPIE: Bellingham, WA, USA, 2006; Volume 6271, p. 62650Z. [CrossRef]
94. Janzen, P.C.; Keas, P.J. Implementation of an active vibration damping system for the SOFIA telescope assembly. In *Proceedings of the Astronomical Telescopes and Instrumentation*; SPIE: Bellingham, WA, USA, 2014; Volume 91452, pp. 91452N-1–91452N-8. [CrossRef]
95. Keas, P.; Dunham, E.; Lampater, U.; Pfüller, E.; Teufel, S.; Roeser, H.-P.; Wiedemann, M.; Wolf, J. *Active Damping of the SOFIA Telescope Assembly*; SPIE: Bellingham, WA, USA, 2012; Volume 8444, pp. 844411-1–844411-15. [CrossRef]
96. Neill, D.; Hileman, E.; Sebag, J.; Gressler, W.; Wiecha, O.; Warner, M.; Andrew, J.; Schoening, B. *Baseline Design of the LSST Telescope Mount Assembly*; SPIE: Bellingham, WA, USA, 2014; Volume 9145, pp. 914518-1–914518-16. [CrossRef]
97. Hartung, M.; Hayward, T.; Saddlemyer, L.; Poyneer, L.; Cardwell, A.; Cavedoni, C.; Cho, M.; Chilcote, K.J.; Collins, P.; Dillon, D. *On-Sky Vibration Environment for the Gemini Planet Imager and Mitigation Effort*; SPIE: Bellingham, WA, USA, 2014; Volume 9148, pp. 91480N-1–91480N-12. [CrossRef]
98. Yao, X.C.; Jiang, C.Y.; Zhao, C.; Zeng, T. Fabrication and Vibration Reduction Effect of Piezoelectric Actuator. *Mater. Mech. Eng.* **2021**, *45*, 89–93. [CrossRef]
99. Zhang, M. Research on Active Vibration Isolation Method Based on Robust Control Theory. Ph.D. Thesis, Harbin Institute of Technology, Harbin, China, 2019. [CrossRef]
100. Qin, C. Research on the Key Technologies of Micro-Vibration Suppression for the Space Telescope. Ph.D. Thesis, Changchun Institute of Optics, Fine Mechanics and Physics, Chinese Academy of Sciences, Changchun, China, 2022. [CrossRef]

101. Jiang, L.H.; Zhu, M.; Qi, S.; Yu, M. Research on magnetorheological three-directional vibration isolator for complex vibration condition. *J. Chongqing Univ.* **2024**, *47*, 1–17. [CrossRef]
102. Wen, L.; Hori, Y. Vibration suppression using single neuron-based PI fuzzy controller and fractional-order disturbance observer. *IEEE Trans. Ind. Electron.* **2007**, *54*, 117–126. [CrossRef]
103. Salton, T.A.; Chen, Z.; Zheng, J.; Fu, M. Constrained optimal preview control of dual-stage actuators. *IEEE/ASME Trans. Mechatron.* **2015**, *21*, 1179–1184. [CrossRef]
104. Bai, Y.D.; Chen, X.; Yang, Z.J. Time-optimal Motion Profile Planning Considering Damping Attenuation for Point to Point Operation. *J. Mech. Eng.* **2019**, *55*, 52–60. [CrossRef]
105. Zhu, X.Y. Research on Precision Positioning Servo Control System Based on Voice Coil Motor. Ph.D. Thesis, University of Chinese Academy of Sciences (Institute of Optics and Electronics, Chinese Academy of Sciences), Chengdu, China, 2022. [CrossRef]
106. Pu, D.L. Rapid Vibration Suppression and High Precision Positioning Control of High Acceleration Air Bearing Motion Systems. Ph.D. Thesis, Shanghai Jiao Tong University, Shanghai, China, 2011.
107. Iwasaki, M.; Yamamoto, M.; Matsui, N. Command shaping for fast and precise positioning considering target position correction. In Proceedings of the 2007 IEEE/ASME international conference on advanced intelligent mechatronics, Zurich, Switzerland, 4–7 September 2007; pp. 1–5. [CrossRef]
108. Gorinevsky, D.; Stein, G. Structured uncertainty analysis of robust stability for multidimensional array systems. *IEEE Trans. Autom. Control.* **2003**, *48*, 1557–1568. [CrossRef]
109. Zhou, C.B.; Xia, M.Y.; Zhang, E.Y.; Xu, Z.B. An array vibration force measuring platform and its test strategy. *Opt. Precis. Eng.* **2022**, *30*, 421–430. [CrossRef]
110. Xia, M.; Zhou, C.; Zhang, E.; Han, C.; Xu, Z. A dynamic disturbance force measurement system based on array sensor for large moving device in spacecrafts. *J. Sound Vib.* **2022**, *535*, 117069. [CrossRef]
111. Zhou, C.; Xia, M.; Xu, Z. A six dimensional dynamic force/moment measurement platform based on matrix sensors designed for large equipment. *Sens. Actuators A Phys.* **2023**, *349*, 114085. [CrossRef]
112. Zhou, C.; Xia, M.; Xu, Z. Design and optimization of a quadrupedal dynamic disturbance force measurement platform using strain gauges. *Mech. Syst. Signal Process.* **2023**, *188*, 110032. [CrossRef]
113. Zhou, C.; Xia, M.; Xu, Z. A piezoelectric load-sharing-based platform for measuring dynamic six-dimensional forces/moments of large equipment in spacecraft. *Precis. Eng.* **2023**, *83*, 112–123. [CrossRef]
114. Zhou, C.; Xu, Z.; Xia, M. Prediction Technique and Measuring Device for Coupled Disturbance Forces from Large Equipment in the Spacecraft. *Sensors* **2024**, *24*, 1284. [CrossRef]
115. Zhou, C.; Xia, M.; Xu, Z. A load-sharing dynamic force measuring platform accounting for inertial force and ambient noise. *Measurement* **2024**, *231*, 114569. [CrossRef]
116. Zhou, C.; Xia, M.; Li, C.; Xu, Z. Structural optimization and dynamic calibration for load sharing dynamic force measurement platform based on MIGA and SVR. *Measurement* **2023**, *218*, 113139. [CrossRef]
117. Zhou, C.; Xia, M.; Xu, Z. Fault-tolerant dynamic force/moment measuring platform for large spacecraft equipment using the GAALBP fusion algorithm. *Mech. Syst. Signal Process.* **2024**, *211*, 111185. [CrossRef]
118. Gao, X. Ground-based Extremely Large Optical Telescope: Technology System, Challenges and Prospects. *J. Space Technol. Eng.* **2025**, *2*, 1–11.

Disclaimer/Publisher's Note: The statements, opinions and data contained in all publications are solely those of the individual author(s) and contributor(s) and not of MDPI and/or the editor(s). MDPI and/or the editor(s) disclaim responsibility for any injury to people or property resulting from any ideas, methods, instructions or products referred to in the content.